



Peer review status:

This is a non-peer-reviewed preprint submitted to EarthArXiv.

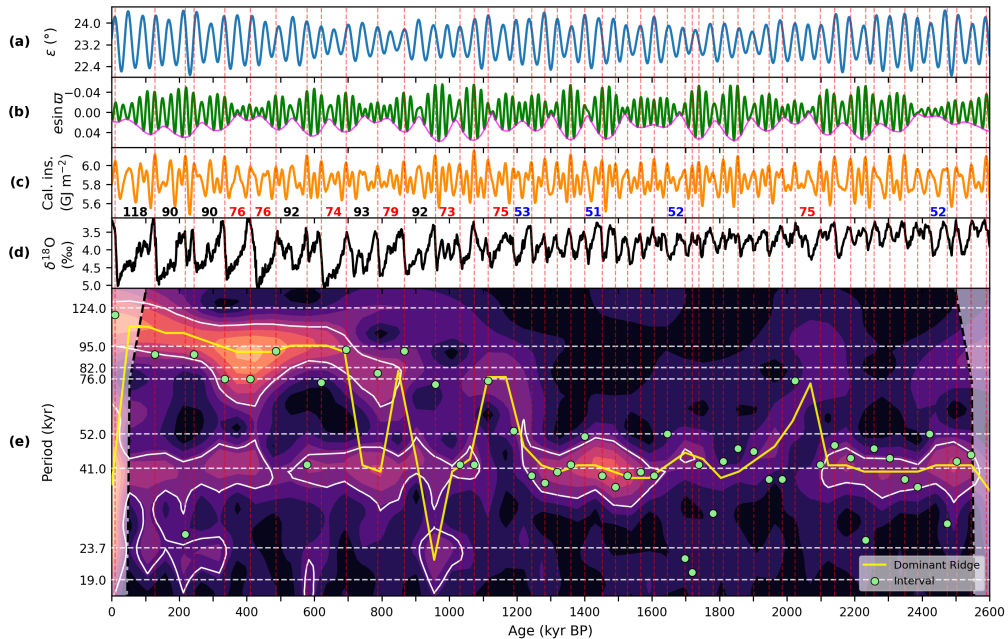


Fig. 1 Orbital forcing and wavelet analyses of the LR04 benthic $\delta^{18}\text{O}$ stack record over the last 2.6 Myr. (a) Obliquity (ε) [10]. (b) Climatic precession ($e \sin \omega$, green) and its eccentricity envelope (e , magenta) [10]. Note that negative values of climatic precession correspond to positive anomalies in Northern Hemisphere summer insolation. (c) Caloric summer half-year insolation at 65°N [11, 12]. (d) LR04 benthic $\delta^{18}\text{O}$ stack record [6]. Higher $\delta^{18}\text{O}$ values indicate larger ice volume and lower deep-ocean temperatures. (e) Wavelet power scalogram of the $\delta^{18}\text{O}$ record. The yellow line indicates the ridge of maximum wavelet power. Areas enclosed by white dashed lines indicate power significant at the 95% confidence level against an AR(1) benchmark. Horizontal dashed lines denote major astronomical periodicities, including the 76-kyr and 52-kyr scales discussed in this study. The vertical dashed lines indicate the timings of insolation peaks associated with interglacial onsets, as defined in Tzedakis et al. (2017) [13], across all panels. Spacings longer than 50 kyr between successive interglacial-inducing insolation peaks are labeled in panel (c). In panel (e), the green dots indicate the insolation-based interglacial spacing (T_{ins}) derived from these peaks.

29 also influenced by deep-sea temperature and salinity [6] (Fig. 1d). Over the course of
 30 long-term Cenozoic cooling, the dominant periodicity of these cycles shifted from ~ 41
 31 kyr to ~ 100 kyr, accompanied by an increase in amplitude—a reorganization known
 32 as the Mid-Pleistocene Transition (MPT; 1.25–0.7 Ma) [7–9].

33 While the astronomical influence on glacial cycles via insolation forcing was pro-
 34 posed as early as the mid-19th century, it lacked robust observational support until
 35 the late 20th century [14]. Hays et al. (1976) [15] provided a breakthrough by per-
 36 forming spectral analysis of marine $\delta^{18}\text{O}$ records, identifying ~ 19 - and ~ 23 -kyr peaks
 37 corresponding to climatic precession (Fig. 1b) and a ~ 41 -kyr peak corresponding to
 38 obliquity (Fig. 1a) [10, 16]. This provided the compelling evidence that glacial cycles
 39 are paced by orbital forcing. However, the ultimate pacemaker of the ~ 100 -kyr cycles
 40 remains controversial; high-latitude summer insolation, considered crucial for the wax-
 41 ing and waning of continental ice sheets, lacks significant power within the ~ 100 -kyr

42 band [14, 15]. Consequently, the ~ 100 -kyr cycles are often interpreted as nonlinear
43 responses occurring once every four or five precession cycles [17–19] or every two or
44 three obliquity cycles [20–22]. It remains a matter of active debate whether precession
45 [19, 23–26], obliquity [20, 21], or a combination of both [13, 22, 27–29] predominantly
46 governs their timing, rhythm, and amplitude.

47 Many studies have investigated the triggers of deglaciations by relating their timing
48 to the phases of obliquity, precession, and various insolation metrics [19, 22, 26, 27, 30].
49 However, uniquely defining the timing of deglaciations is inherently challenging, as the
50 process sometimes spans multiple precession cycles and involves several discrete stages
51 of ice-sheet retreat (see below). Although spectral analysis avoids these timing ambi-
52 guities, it often lacks the resolution required to distinguish spectral peaks sufficiently
53 to resolve the precession-versus-obliquity debate at the ~ 100 -kyr scale.

54 Here, we revisit the spectral analysis of glacial-interglacial cycles using a weighted
55 wavelet spectral analysis method, originally developed by Foster (1996) as the
56 Weighted Wavelet Z-transform [31] and refined by Kirchner and Neal (2013) [32].
57 This approach estimates spectral power via a localized weighted least-squares pro-
58 jection (see Methods). Implemented via the Python package `Pyleoclim` [33], this
59 method resolves both the time-evolving nature of dominant periodicities (scalogram)
60 and the overall power spectral density (PSD) without requiring prior interpolation or
61 detrending. Beyond well-established spectral components, our analysis reveals a dis-
62 tinct ~ 76 -kyr peak (post-1.25 Ma) and a 52-kyr power band (pre-1 Ma) across multiple
63 benthic stacks—findings further corroborated by conventional spectral estimators.
64 Drawing on the theoretical framework of Tzedakis et al. (2017) [13], we interpret these
65 periodicities as robust evidence of nonlinear subharmonic (many-to-one) responses of
66 glacial cycles to climatic precession forcing.

67 Wavelet spectral analysis of benthic $\delta^{18}\text{O}$ records

68 Wavelet-based spectral analysis is performed on seven benthic $\delta^{18}\text{O}$ records (Fig. S1) to
69 investigate their periodicities under varying age-modeling constraints (see Methods).
70 First, we include the orbitally-tuned LR04 stack [6] (Fig. 1d) and its orbital-tuning-
71 free counterpart in Lisiecki (2010) [34]. Second, we analyze recent stack records in
72 Zhou et al. (2026) [35]: `BIGSTACKmixed` uses speleothem-based age constraints for
73 0–654 ka and tuning to an ice-sheet model for earlier intervals; `BIGSTACKmagrev` is
74 primarily constrained by paleomagnetic events to minimize orbital circularity; and
75 `BIGSTACKauto` is generated using an automated optimization algorithm [36] to min-
76 imally tune to the pervasive 41-kyr obliquity cycle, while avoiding assumptions about
77 astronomical phase relationships. Additionally, we utilize the orbitally-untuned ben-
78 thic stack record in Huybers (2007) [37] and the paleomagnetically-constrained record
79 U1476pMag from IODP Site U1476 [25]. To ensure the robustness of the detected peri-
80 odicities, we primarily focus on results from records with minimal or no orbital tuning
81 (Lisiecki 2010, `BIGSTACKmagrev`, Huybers 2007, and U1476pMag), while using the
82 fully tuned records as supplementary evidence.

83 The result of time-frequency analysis for the orbitally tuned LR04 record is shown
84 in Fig. 1e, with the yellow line tracking the instantaneous period at which the wavelet

85 amplitude is maximized (see Figs. S2–S7 for the other records). The evolution of the
86 dominant period in the seven records compared in Fig. 2 exhibits a broadly similar
87 pattern across all analyzed records, although the MPT epoch (0.7–1.25 Ma) is notably
88 complex, with marked discrepancies between records.

89 Prior to the MPT, the dominant period remains centered near 41 kyr, although
90 most records show transient increases in the primary period between 1.8 and 2.1 Ma
91 (Fig. 2), with some variability in timing among the stacks. At the onset of the MPT,
92 the dominant period increases up to ~ 76 kyr by ~ 1.2 Ma, a feature robust across
93 records. However, this increase is interrupted around 1.1 Ma, and the subsequent
94 evolution of the dominant period during 1.1–0.7 Ma varies significantly among the
95 records. Notably, the dominant period retreats to ~ 22 kyr in the tuned and untuned
96 LR04 records and to ~ 41 kyr in the other records at least once during 1.1–0.9 Ma.
97 This transient reduction in period coincides with the strongest eccentricity maximum
98 of the Quaternary. While the emergence of strong ~ 100 -kyr power after ~ 700 ka is well
99 documented [38–40], our analysis uncovers a more nuanced progression. Specifically,
100 the dominant period remains centered near ~ 95 kyr over 700–300 ka, after which it
101 lengthens toward ~ 120 kyr (Fig. 2). The temporal evolution of the dominant period of
102 ice age cycles closely follows that of eccentricity, excluding the ~ 400 -kyr component,
103 suggesting the establishment of frequency locking between ice volume and ~ 100 -kyr-
104 scale eccentricity cycles after the end of the MPT (~ 700 ka) (Fig. 2c).

105 To assess the statistical significance of the observed periodicities, we calculate
106 power spectral densities (PSDs) for the intervals before and after the MPT. For the
107 mid-to-late Pleistocene (the past 1.25 Myr), 95-kyr, 41-kyr, and 23-kyr periodicities
108 generally exhibit significant power at the 95% confidence level, although the latter two
109 do not reach this level in the U1476 record (Fig. 3). Notably, we identify a spectral peak
110 near ~ 76 kyr, which is significant in all records—including the orbitally tuned LR04
111 (at the 90% level) and U1476—except for the untuned LR04. However, conventional
112 periodograms (Fig. S9) reveal significant ~ 76 -kyr peaks across all records, including
113 the untuned LR04. While this peak is less defined in Lomb–Scargle periodograms
114 over the last 1.25 Myr, it becomes significant when the analysis is extended to the
115 full Quaternary (2.6 Myr) except the untuned LR04 (Fig. S10). During the early-to-
116 mid Pleistocene (1.0–2.6 Ma), the 41-kyr spectral peak is prominent across all records
117 (Fig. 4). The tuned LR04 record further exhibits a significant peak at ~ 52 kyr, while
118 the PSDs of BIGSTACK_{magrev} and Huybers (2007) show a significant shoulder extend-
119 ing from the 41-kyr peak toward this periodicity. A similar, though non-significant
120 ($< 95\%$), feature is present in the untuned LR04. In contrast, no comparable 52-kyr
121 power is observed in BIGSTACK_{mixed}, BIGSTACK_{auto}, and U1476pMag. Given that
122 BIGSTACK_{auto} and BIGSTACK_{magrev} share the same $\delta^{18}\text{O}$ values but employ dif-
123 ferent age-modeling strategies, it is possible that the ~ 52 -kyr power was suppressed
124 or lost during the orbital tuning process to the 41-kyr obliquity cycles. Regarding
125 U1476pMag, the absence of ~ 52 -kyr power likely stems from its relatively short record
126 length (786.5 kyr), which limits the spectral resolution required to resolve such com-
127 ponents. Consistently, alternative estimators—specifically conventional (Fig. S9) and
128 Lomb–Scargle periodograms (Fig. S10)—detect the ~ 52 -kyr feature in most records,
129 reinforcing its robust presence.

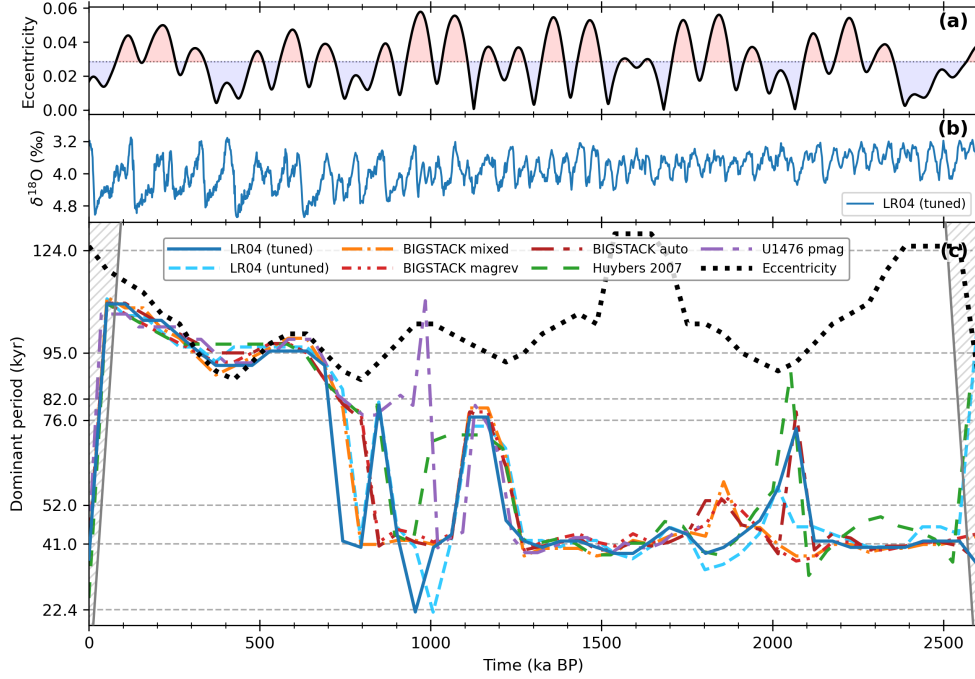


Fig. 2 Evolution of the dominant timescale of glacial cycles and that of eccentricity. (a) Eccentricity. The horizontal is the average. (b) LR04 benthic $\delta^{18}\text{O}$ stack. (c) Dominant timescale corresponding to the maximum wavelet amplitude at each time. Horizontal dashed lines denote major astronomical periodicities, including the 76-kyr and 52-kyr scales discussed in this study.

130 In summary, spectral power near ~ 76 kyr and ~ 52 kyr is reproducible across mul-
 131 tiple datasets and estimation methods, though detectability varies with age modeling
 132 and tuning strategies. The ~ 76 -kyr peak is a consistent feature of late Pleistocene
 133 variability, while the ~ 52 -kyr feature—despite less consistent expression—appears to
 134 be a real component of early-to-mid Pleistocene variability rather than an analytical
 135 artifact. The lack of detection in the untuned LR04 likely reflects its conservative age
 136 constraints using only three tie points over the 2.6 Myr [34] (Methods), which may
 137 dampen these specific periodicities.

138 Interpretation of ~ 76 -kyr and ~ 52 -kyr components

139 We interpret the periodicities detected in the PSD in relation to insolation cycles,
 140 using the theoretical framework of interglacial spacing proposed by Tzedakis et al.
 141 (2017) [13] (T17). In this model, an interglacial occurs when the caloric summer half-
 142 year insolation peak at 65°N exceeds a threshold that declines with the time elapsed
 143 since the previous interglacial, reflecting the accumulated instability during the glacial
 144 period (Methods). Using this criterion, the model predicts which insolation peaks lead
 145 to interglacials over the Quaternary (Fig. 1, vertical dashed lines). Though BIGSTACK

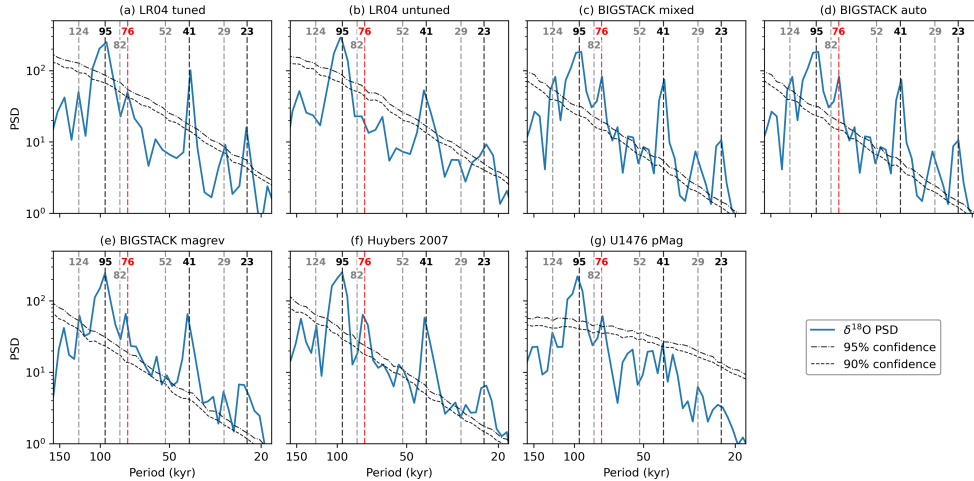


Fig. 3 Power spectral densities (PSD) of benthic $\delta^{18}\text{O}$ records over the last 1.25 Myr. (a) the tuned LR04 stack [6], (b) the untuned LR04 stack [34], (c) $\text{BIGSTACK}_{\text{mixed}}$ [35], (d) $\text{BIGSTACK}_{\text{auto}}$ [35], (e) $\text{BIGSTACK}_{\text{magrev}}$ [35], (f) the untuned record from Huybers (2007) [37], and (g) the U1476 record [25]. Solid blue lines denote the PSD of the $\delta^{18}\text{O}$ records, and dashed/dotted black lines indicate the 95% and 90% confidence levels against an AR(1) benchmark. Vertical dashed lines highlight key periodicities: eccentricity (124 and 95 kyr), obliquity (41 kyr), and climatic precession (23 kyr). Also indicated are the subharmonic of 41 kyr (82 kyr), the combination tone (29 kyr; $1/29 \approx 1/41 + 1/95$) [41], and specific timescales of interest in this study (76 and 52 kyr).

146 was recently published [35] as an update to LR04, we use LR04 in the following analysis
 147 because the T17 model was calibrated using that stack.

148 We calculate proxy-based deglaciation spacings and insolation-based interglacial
 149 spacings, demonstrating their overall consistency. Following T17, interglacials are identified
 150 in the LR04 record when $\delta^{18}\text{O}$ values fall below a predefined threshold (see
 151 Methods). Near each threshold-crossing timing of $\delta^{18}\text{O}$, the timing of deglaciation
 152 is specified as the peak in the derivative of the 10-kyr smoothed LR04 $\delta^{18}\text{O}$ record
 153 (Figs. S11–S13). Some deglaciations span multiple precession cycles, leaving multiple
 154 peaks in $\delta^{18}\text{O}$ derivative (e.g., deglaciations leading to MIS 13a near 500 ka as well
 155 as MIS 17 near 700 ka in Fig. S11). We select the largest derivative peak within a
 156 window of either ± 10 kyr or ± 15 kyr around each threshold-crossing point. The ± 10 -
 157 kyr window tends to capture the later peak within a deglaciation sequence, whereas
 158 the ± 15 -kyr window captures the earlier peak (Figs. S11–S13). The resulting spacings
 159 between deglaciations, denoted T_{later} and T_{earlier} , are shown in Fig. 5. Furthermore, we
 160 define insolation-based interglacial spacing (T_{ins}) as the intervals between successive
 161 caloric summer insolation peaks that ultimately induced each interglacial [13] (Fig. 5;
 162 Fig. 1e, green dots). The $\delta^{18}\text{O}$ -derivative-based intervals may tightly couple with the
 163 periodicities detected in the PSD, but their values rely on an assumed age model. In
 164 contrast, the insolation-based intervals are relatively free from chronological uncer-
 165 tainties and can be directly linked to orbital cycles. See Supplementary Data S1 for
 166 the values of T_{later} , T_{earlier} , and T_{ins} .

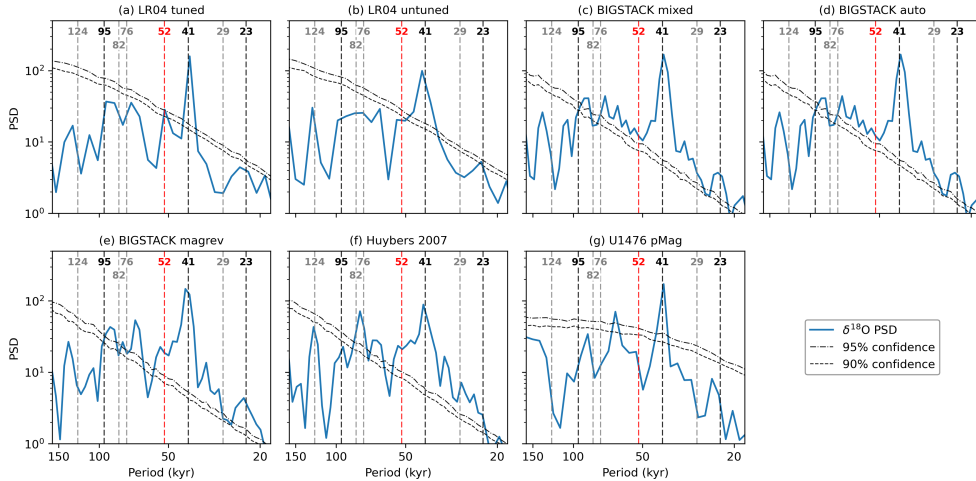


Fig. 4 Power spectral densities (PSD) of benthic $\delta^{18}\text{O}$ records over 1.0–2.6 Ma. (a) the tuned LR04 stack [6], (b) the untuned LR04 stack [34], (c) $\text{BIGSTACK}_{\text{mixed}}$ [35], (d) $\text{BIGSTACK}_{\text{auto}}$ [35], (e) $\text{BIGSTACK}_{\text{magrev}}$ [35], (f) the untuned record from Huybers (2007) [37], and (g) the U1476 record [25]. Solid blue lines denote the PSD of the $\delta^{18}\text{O}$ records, and dashed/dotted black lines indicate the 95% and 90% confidence levels against an AR(1) benchmark. Vertical dashed lines highlight key periodicities: eccentricity (124 and 95 kyr), obliquity (41 kyr), and climatic precession (23 kyr). Also indicated are the subharmonic of 41 kyr (82 kyr), the combination tone (29 kyr; $1/29 \approx 1/41 + 1/95$) [41], and specific timescales of interest in this study (76 and 52 kyr).

167 The high consistency among T_{later} , T_{earlier} , and T_{ins} shown in Fig. 5a ($r \gtrsim 0.95$,
168 $\text{RMSE} \lesssim 6.5$ kyr) supports T_{ins} as a reliable basis for analyzing glacial-cycle periodicities.
169 Although discrepancies of up to ~ 20 kyr exist for certain deglaciations—likely
170 reflecting the inherent uncertainty in deglaciation timing and the simplified nature
171 of the T17 model—the overall robustness of the correlation supports using T_{ins}
172 for interpreting the periodicities in the PSD.

173 The distribution of T_{ins} shows clear clustering around 90–93 kyr and 73–76 kyr
174 (Fig. 5e). A similar, albeit weaker, clustering is preserved in T_{earlier} (Fig. 5d). We,
175 therefore, attribute the ~ 95 -kyr spectral peak to the cluster of 90–93 kyr spacings, and
176 the ~ 76 -kyr spectral peak to the 73–76 kyr cluster. Before the MPT (~ 1.2 Ma), T_{ins} is
177 distributed around the 41-kyr obliquity period with a mean of 41.2 kyr, contributing
178 to the dominant 41-kyr peak. However, its standard deviation is substantial (± 10 kyr).
179 Indeed, four spacings fall within 51–53 kyr (Figs. 1e, 5e), contributing to the significant
180 ~ 52 -kyr peak in the PSD of the LR04 record over 1.0–2.6 Ma (Fig. 4a).

181 Once linked with T_{ins} , the observed spectral peaks can be traced back to their
182 physical origins by decomposing the insolation forcing into climatic precession and
183 obliquity components. A key factor in considering the variability of T_{ins} is that the
184 duration of climatic precession cycles varies widely between 14 and 31 kyr when eccen-
185 tricity is low, whereas it remains relatively stable around 22.1 kyr when eccentricity
186 is high (Fig. S14) [42]. Indeed, the length of the late-Pleistocene glacial cycles is
187 explained with the varying durations of climatic precession cycles [19]. Building on

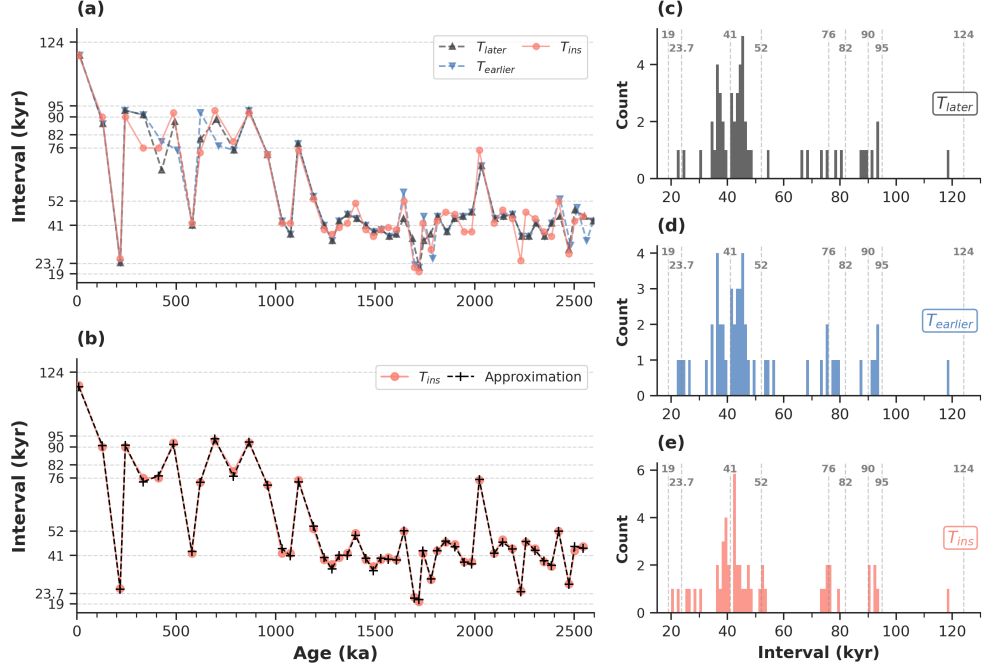


Fig. 5 Comparison of proxy-based deglaciation spacings and insolation-based interglacial spacings. (a) Time series of spacings over the past 2600 kyr. These intervals are defined by three different metrics: orbital insolation peaks (T_{ins} , salmon circles) and the timing of peak deglaciation rates (T_{later} , dark blue triangles; $T_{earlier}$, light blue inverted triangles). Horizontal dashed lines indicate key orbital periodicities and the sub-harmonic periodicities discussed in this study (52, 76, and 82 kyr). (b) Comparison between the insolation-based spacings (T_{ins}) and their theoretical approximation (black crosses). (c)–(e) Frequency distributions (histograms) of (c) T_{later} , (d) $T_{earlier}$, and (e) T_{ins} . The insolation-based distribution (e) exhibits distinct clustering around 73–76 kyr and 90–93 kyr; this pattern is partially reflected in the $T_{earlier}$ and T_{later} metrics. All proxy-based metrics align well with T_{ins} ($r \gtrsim 0.95$, $RMSE \lesssim 6.5$ kyr), justifying the use of T_{ins} as a robust theoretical framework for spectral analysis.

188 this, we derive more refined relationships between T_{ins} and the evolving durations of
 189 precession and obliquity cycles.

190 For each glacial cycle, we approximate the local variations in the caloric summer
 191 half-year insolation as $f(t) = A_p \cos(\omega_p t + \varphi_p) + A_o \cos(\omega_o t + \varphi_o)$, accounting for the
 192 respective positive contributions of climatic precession and obliquity to the insolation.
 193 Here, $A_{p,o}$ are the local-mean amplitudes, $\omega_{p,o}$ are the angular frequencies (correspond-
 194 ing to local-mean periods $T_{p,o}$), and $\varphi_{p,o}$ are the local phases of climatic precession
 195 and obliquity cycles. Unless otherwise noted, we can choose $A_{p,o} = 1$ for 65°N caloric
 196 summer insolation, as climatic precession and obliquity contribute nearly equally to
 197 the total variance [11]. The local-mean periods T_p (T_o) are calculated from the time
 198 intervals between successive precession minima (obliquity maxima) associated with

199 deglaciations (Figs. S15–S18; Data S1). The local phases $\varphi_{p,o}$ are chosen from the dis-
 200 crete set $\{0, \pm\pi/2, \pi\}$ for simplicity, to best capture local insolation variations. Then,
 201 we obtain approximation formulae for T_{ins} as follows.

Here we present two representative cases (all derivations are provided in the Sup-
 plementary Information). When the peaks of climatic precession and obliquity nearly
 coincide and collectively induce an interglacial, we define this peak time as $t = 0$ by
 setting $\varphi_p = \varphi_o = 0$ (Fig. S19a). If the spacing T_{ins} between the peak at $t = 0$ and a
 subsequent interglacial-inducing peak is close to the n -th multiple of the local-mean
 precession period T_p , it can be expressed as $T_{\text{ins}} = nT_p + \delta$. Here, δ represents a small
 temporal shift relative to the nominal insolation peak, originating from the modulation
 by obliquity. By linearizing the peak condition as $f'(nT_p + \delta) \approx f'(nT_p) + f''(nT_p)\delta = 0$,
 we obtain approximation formulae for T_{ins} ($n = 2, 3, 4, 5$), called type-a:

$$T_{\text{ins}} \approx nT_p - \frac{A_o\omega_o \sin(n\omega_o T_p)}{A_p\omega_p^2 + A_o\omega_o^2 \cos(n\omega_o T_p)}.$$

202 An example of type-a is the ~ 76 -kyr spacing between interglacials MIS 11c and MIS 9e
 203 (Fig. S15), where the corresponding insolation peaks are separated by approximately
 204 four precession cycles ($n = 4$), and the local-mean precession period is $T_p = 18.25$ kyr.
 205 Furthermore, the local-mean obliquity period is $T_o = 41.5$ kyr. The type-a formula
 206 then predicts $T_{\text{ins}} = 74.3$ kyr. This value is closer to the actual value of 76 kyr than the
 207 simple multiple of precession, $nT_p = 73$ kyr, obtained without the shift $\delta = 1.43$ kyr.

The second case occurs when a glacial cycle spans roughly three precession cycles
 ($n = 3$); here, the insolation is locally approximated as $f(t) = -A_p \cos(\omega_p t) -$
 $A_o \cos(\omega_o t)$ over the interval $-\frac{3}{2}T_p \lesssim t \lesssim \frac{3}{2}T_p$ corresponding to $\varphi_p = \varphi_o = \pi$
 (Fig. S19b). For this case, we assume that deglaciations occur at $t = \pm(\frac{3}{2}T_p + \delta)$, with
 δ being a small obliquity-induced shift. Following a derivation similar to that of the
 type-a formulae, T_{ins} is given by the following formula (type-3b):

$$T_{\text{ins}} \approx 3T_p + \frac{2A_o\omega_o \sin(\frac{3}{2}\omega_o T_p)}{A_p\omega_p^2 - A_o\omega_o^2 \cos(\frac{3}{2}\omega_o T_p)}.$$

208 An example of type-3b is the spacing between interglacials MIS 37 and MIS 35
 209 (Fig. S16). The corresponding insolation peaks are separated by approximately three
 210 precession cycles, and the local-mean precession period is $T_p = 19$ kyr. Furthermore,
 211 the local-mean obliquity period is $T_o = 39$ kyr. Then, the type-3b formula predicts
 212 $T_{\text{ins}} = 54.2$ kyr. This value is closer to the actual value of 53 kyr than the simple
 213 multiple of precession, $nT_p = 57$ kyr, obtained without the shift $\delta = -2.8$ kyr.

214 In this manner, by varying the number of precession cycles (n) and the local
 215 phases $\varphi_{p,o}$, we derive twelve distinct formulae (e.g., types 2a–5a, 1b–4b, 1c–2c, 2d,
 216 and pp). The detailed derivation of each formula is presented in the Supplementary
 217 Information, along with a one-to-one correspondence to each individual glacial cycle
 218 (Table S1). These analytical expressions account for nearly 50 interglacial spacings
 219 identified throughout the Quaternary. While we generally use a fixed amplitude ratio
 220 of $A_p/A_o = 1$ for simplicity, we explicitly consider the relative amplitudes in two

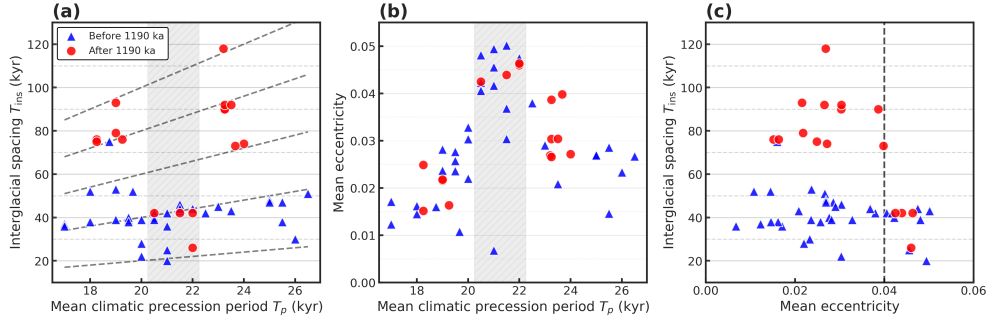


Fig. 6 Statistical relationships between orbital parameters and interglacial spacings. (a) Mean climatic precession period (T_p) versus the insolation-based interglacial spacing (T_{ins}). Dashed lines represent integer multiples of T_p ($T = nT_p$ for $n = 1, \dots, 5$), showing the clustering of interglacial spacing. (b) T_p versus the mean eccentricity (\bar{e}) over each interval. In (a) and (b), the vertical hatched area (20.25–22.25 kyr) indicates the range of climatic precession periods where high mean eccentricity generally prevents the skipping of precession peaks. (c) Mean eccentricity versus T_{ins} . The vertical dashed line at $\bar{e} = 0.04$ indicates the threshold below which peak-skipping (longer T_{ins}) becomes frequent. In all panels, blue triangles and red circles represent intervals before and after 1190 ka, respectively.

221 specific cases of extremely low eccentricity (MIS 99–97 and MIS 97–95). Similarly, the
 222 intervals MIS 95–93 and MIS 93–91 represent epochs in which eccentricity remains
 223 near zero. The aforementioned formulae are inapplicable to these events as deglaciation
 224 aligns with the obliquity maximum at 2386 ka, where eccentricity is virtually zero. For
 225 these two cases, we employ exceptional but simplified estimates for T_{ins} , the details of
 226 which are described in the Supplementary Information. The validity of this analytical
 227 framework is confirmed by its high predictive power; across the entire Quaternary,
 228 these formulae approximate T_{ins} with a mean absolute error of only 0.8 kyr (Fig. 5b).

229 Precession phase-locking and forbidden periodicities

230 It is found that the shift δ in the approximation $T_{\text{ins}} = nT_p + \delta$ has standard deviation
 231 of only 2.7 kyr. Consequently, the insolation-based interglacial spacings T_{ins} cluster
 232 along the lines $T_{\text{ins}} = nT_p$ ($n = 1, 2, 3, 4, 5$) as functions of the local-mean precession
 233 period T_p (Fig. 6a). The number of precession cycles within each interglacial spacing,
 234 n , can be explained by the T17 theory [13], where a longer spacing $T_{\text{ins}} (\approx nT_p)$
 235 facilitates crossing the deglaciation threshold due to the accumulated instability of the
 236 ice sheet–climate system due to the accumulated instability of the ice sheet–climate
 237 system (see Methods). After the onset of the MPT around 1.2 Ma, n statistically
 238 increases as a result of an elevated deglaciation threshold, and the points (T_p, T_{ins})
 239 tend to cluster along higher branches with $n \geq 3$.

240 Figure 6a reveals that similar interglacial spacings (T_{ins}) can arise from different
 241 precession-cycle lengths (T_p). For instance, the 90–93 kyr spacings comprise either four
 242 precession cycles with a mean period of $T_p \approx 23$ kyr or five cycles with a mean period
 243 of $T_p \approx 19$ kyr. Similarly, the 73–76-kyr spacings comprise either three precession
 244 cycles with a mean period of $T_p \approx 24$ kyr or four precession cycles with a mean

245 period of $T_p \approx 19$ kyr. A similar bifurcation is observed for the 51–53-kyr spacings,
 246 which split into two distinct solutions: three multiples of precession cycles with a mean
 247 period of $T_p \approx 19$ kyr and two multiples of precession cycles with a mean period of
 248 $T_p \approx 26.5$ kyr. The points in ~ 41 -kyr cluster distribute along $T_{\text{ins}} = 2T_p$ (Fig. 6a, the
 249 second dashed line from the bottom), showing the persistent influence of precession
 250 cycles across the MPT, as suggested in previous studies [25, 43–45].

251 Interestingly, when the mean climatic precession period T_p falls between 20.5 and
 252 22 kyr, glacial cycles longer than 50 kyr are notably absent (shaded region, Fig. 6a).
 253 This gap occurs because this intermediate T_p range coincides with periods of high
 254 mean eccentricity ($\bar{e} > 0.04$) both after and, in many cases, before the MPT’s onset
 255 (~ 1.2 Ma) (Fig. 6b). Under these conditions of high eccentricity, the amplified climatic
 256 precession forcing ensures that summer insolation remains sufficiently high to trigger
 257 deglaciation within one or two precession cycles (Fig. 6c), thereby precluding longer
 258 cycles. This orbital constraint provides a physical basis for the distinct gaps observed
 259 in the spacing histograms (Figs. 5c–5e), explaining why certain durations— ~ 60 – 66
 260 kyr (3×20 to 3×22) and ~ 100 – 110 kyr (5×20 to 5×22)—are effectively precluded.

261 Discussion

262 We show that glacial cycles evolved from a quasi-41-kyr regime characterized by large
 263 variability—including ~ 52 -kyr cycles—to quantized ~ 76 , ~ 95 , and ~ 120 -kyr cycles.
 264 This points to precession-based pacing as a persistent feature of glacial dynamics
 265 throughout the Quaternary. Following the onset of the MPT (~ 1.2 Ma), ~ 76 -kyr cycles
 266 emerged, coinciding with the disappearance of the ~ 52 -kyr periodicity. After the first
 267 ~ 92 -kyr cycle appeared at ~ 0.9 Ma, the dominant period stabilized around ~ 95 kyr
 268 from ~ 700 to ~ 300 ka, before eventually lengthening toward ~ 120 kyr. This temporal
 269 evolution of the dominant period closely tracks the ~ 100 -kyr eccentricity component
 270 (excluding the 400-kyr cycle), suggesting that frequency-locking between ice volume
 271 and eccentricity was established after the end of the MPT (~ 700 ka; Fig. 2c). Such
 272 resonance between the internal climate response and orbital forcing may explain the
 273 abrupt increase in 100-kyr cycle amplitude observed at approximately 650 ka [38].

274 While the prominence of the ~ 76 -kyr periodicity has been noted in several studies
 275 [19, 46, 47], its physical origin has remained elusive. For instance, Bolton et al. (1995)
 276 [46] identified ~ 75 -kyr power around 750 ka but attributed it to internal variability,
 277 citing the lack of a corresponding periodicity in the astronomical forcing. Rial (1999)
 278 [47] proposed that the ~ 75 -kyr peak is a sideband frequency ($1/77 \approx 1/95 + 1/413$)
 279 generated by frequency modulation of the 95-kyr cycle by the 413-kyr eccentricity
 280 component; however, the physical basis for such modulation remains elusive. In
 281 contrast, our results demonstrate that the ~ 76 -kyr spectral power arises from sub-
 282 harmonic phase-locking to either three precession cycles (mean period $T_p \approx 24$ kyr)
 283 or four precession cycles ($T_p \approx 19$ kyr), with only a minor contribution from obliq-
 284 uity modulation. Consistently, Blackburn et al. (2024) [19] attributed the spacings
 285 from MIS 13a to 11c and 11c to 9e to the 76-kyr mode of four precession cycles. This
 286 precession-based 76-kyr mode is distinct from the previously proposed ~ 70 -kyr vari-
 287 ability, which was interpreted as a beat frequency between obliquity and eccentricity

288 (1/70 \approx 1/41 – 1/100) [41]. Within our present same framework, the \sim 95-kyr spectral
289 power can also be explained as a result of subharmonic phase-locking to either four
290 ($T_p \approx$ 23 kyr) or five ($T_p \approx$ 19 kyr) precession cycles [17–19, 23, 26, 48].

291 While the dominant power prior to the MPT is often characterized as \sim 41 kyr [49],
292 this represents only a statistical average. In reality, interglacial spacings exhibit large
293 variations of \sim 10 kyr around this mean because they correspond to either two or three
294 multiples of climatic precession cycles, whose periods themselves vary significantly.
295 Such variability in glacial duration is indeed reproduced in a mathematical model or
296 a climate-ice sheet model [44, 50]. Our analysis identifies the \sim 52-kyr-scale spectral
297 shoulder extending from the 41-kyr peak as a diagnostic signature of this precessional
298 influence prior to the onset of the MPT (\sim 1.2 Ma). Previous research [41] attributed
299 the spectral peaks near 50 kyr and 55 kyr to an eccentricity overtone (1/50 = 2/100
300 kyr $^{-1}$) and an obliquity sideband, respectively. In contrast, we focus on the 51–53 kyr
301 band and attribute its origin to a nonlinear subharmonic response. This is character-
302 ized by two distinct solutions: the system responding once for every three precessional
303 cycles of a mean period of $T_p \approx$ 19 kyr or once for every two cycles of a mean period
304 of $T_p \approx$ 26.5 kyr.

305 The presence of bundles of precession cycles— \sim 52-kyr cycles before \sim 1.2 Ma,
306 \sim 76-kyr cycles after \sim 1.2 Ma, and \sim 95-kyr cycles after \sim 0.9 Ma—throughout the
307 Pleistocene suggests that the MPT was not a disappearance of the obliquity-driven 41-
308 kyr world, but rather a progressive shift in the skipping behavior of precession-paced
309 deglaciations. This persistent influence of precession cycles both before and after the
310 MPT is consistent with recent findings [25, 43–45, 51].

311 Consequently, the MPT can be understood as a period-adding process in
312 precession-phase locking, driven by a gradual increase in the deglaciation threshold
313 in the coupled ice-sheet–ocean–carbon system. The threshold likely increased grad-
314 ually through long-term global cooling, declining atmospheric CO₂ toward critical
315 minima [52–54], and structural changes in the cryosphere system including progressive
316 removal of subglacial regolith beneath Northern Hemisphere ice sheets [54–56], expan-
317 sion of marine-based Antarctic ice sheets [57], long-term AMOC slowdown [58], and
318 enhanced stratification of the Southern Ocean [59]. These processes may have con-
319 tributed to increasing the intrinsic timescale of the climate–ice-sheet system [28, 60],
320 although their relative roles and interactions remain poorly constrained. Identifying
321 the underlying physical mechanisms of the MPT is beyond the scope of this study.

322 We found that when the local-mean precession period T_p falls within this inter-
323 mediate range (20.5–22 kyr), high eccentricity triggers deglaciation, precluding the
324 emergence of \sim 100–110-kyr and \sim 60–65-kyr cycles. This is consistent with previous
325 findings of an anticorrelation between \sim 100-kyr eccentricity power and \sim 100-kyr ice-
326 age power [44, 61]. Our analysis shows that mean eccentricity does not exceed 0.04
327 during the observed \sim 100-kyr cycles (Fig. 6c). This implies that the development of
328 \sim 100-kyr cycles was precluded during the high-eccentricity interval between \sim 950 and
329 1100 ka. Consequently, the onset of the MPT—specifically the lengthening of glacial
330 cycles—appears to have been constrained by the long-term evolution of eccentricity
331 [9, 44].

332 Our findings refine the conventional paradigm of a simple transition from a 41-
333 kyr world to a 100-kyr world across the MPT. Instead, we propose a more nuanced
334 evolution: from a quasi-41-kyr regime characterized by high orbital variability to a
335 suite of quantized cycles (~ 76 , ~ 95 , and ~ 120 kyr) linked to precession phases. In
336 this framework, obliquity determines which climatic precession peaks are skipped, as
337 suggested in several studies [13, 19, 27, 28].

338 Methods

339 Benthic $\delta^{18}\text{O}$ records

340 We analyze seven benthic $\delta^{18}\text{O}$ records (Fig. S1) categorized by their degree of orbital
341 tuning. The first is the standard, orbitally-tuned LR04 stack [6] (Fig. 1d). The sec-
342 ond is the tuning-free version of the LR04 stack from Lisiecki (2010) [34], which
343 assumes a constant sedimentation rate between three primary tie points: the core top
344 (0 ka) and the geomagnetic reversals at 0.78 and 2.58 Ma. Third through fifth, we uti-
345 lize three versions of the BIGSTACK from Zhou et al. (2026) [35]: BIGSTACK_{mixed}
346 integrates 221 global records using speleothem-based age constraints for 0–654 ka
347 and ice-sheet model tuning for earlier intervals. BIGSTACK_{magrev} (comprising 33
348 records) is constrained by 15 paleomagnetic events over the last 2.606 Ma to minimize
349 orbital circularity. BIGSTACK_{auto} is derived from BIGSTACK_{magrev} by applying the
350 eTimeOpt algorithm [36, 62] to minimally tune the pervasive 41-kyr obliquity signal
351 without assuming astronomical phase relationships. The sixth record is the depth-
352 derived stack of Huybers (2007) [37]. While the original study focuses on the last 2 Ma,
353 the dataset provides a tuning-free chronology anchored to the 2.58 Ma geomagnetic
354 boundary (<https://doi.org/10.25921/d1zr-t492>, last accessed 8 April 2026). Lastly, we
355 include the single-site benthic $\delta^{18}\text{O}$ record from IODP Site U1476, anchored to an
356 independent paleomagnetic age model (U1476pMag) [25]. Because this record spans
357 only the last 1786.542 kyr, its coverage of the pre-MPT interval (1.0–1.79 Ma) is rel-
358 atively short. Consequently, the presence or absence of periodicities in this specific
359 epoch should be interpreted with caution due to the limited duration of the time series.

360 In our spectral analysis, periodicities are primarily accepted based on the tuning-
361 free records (Lisiecki 2010, Huybers 2007, and U1476pMag) and the minimally-tuned
362 BIGSTACK_{magrev}. The orbitally-tuned records (standard LR04, BIGSTACK_{mixed},
363 and BIGSTACK_{auto}) are used as supplementary evidence to support the robustness
364 of the detected signals.

365 Wavelet-based spectral analysis

366 Paleoclimate time series are commonly unevenly sampled, which complicates the
367 application of conventional spectral estimators, such as the periodogram [63] and
368 the multitaper method spectrum [64]. Standard approaches often rely on interpola-
369 tion to a regular time grid prior to analysis; however, such interpolation acts as a
370 low-pass filter, leading to a reddening of the power spectrum and, consequently, spu-
371 rious results in hypothesis testing [65]. While the Lomb–Scargle periodogram [66, 67]

372 avoids interpolation, it is known to overestimate power at high frequencies [65]. More-
 373 over, Fourier-based methods, which assume stationarity, necessitate data detrending
 374 [68]. However, even with recent methodological advances, identifying and removing a
 375 trend without inadvertently compromising the underlying climate signal remains an
 376 inherently difficult task [69].

377 To overcome these difficulties, we employ a weighted wavelet spectral analysis
 378 method. This approach, originally developed by Foster (1996) [31] as the Weighted
 379 Wavelet Z-transform (WWZ) and subsequently refined by Kirchner and Neal (2013)
 380 [32], estimates spectral power via weighted least-squares projection. This approach,
 381 implemented in the Python package `Pyleoclim` [33], enables the resolution of both
 382 the time-evolving nature of dominant periodicities (scalograms) and the overall fre-
 383 quency content (power spectral density; PSD) without requiring prior interpolation
 384 or detrending.

385 The method estimates time-dependent harmonic amplitudes (a_1, a_2) through local-
 386 ized fits of sinusoidal functions and a constant to the data using weighted least squares
 387 [32]. Specifically, for each center time t^* and angular frequency ω , the coefficients a_1
 388 and a_2 are obtained by fitting: $x_i = a_0 + a_1 \cos[\omega(t_i - t^*)] + a_2 \sin[\omega(t_i - t^*)]$, where each
 389 observation x_i at time t_i is weighted by a Gaussian weight $w_i = \exp[-c\omega^2(t_i - t^*)^2]$,
 390 with a decay constant c controlling the time-frequency resolution trade-off. However,
 391 when the data are unevenly sampled in time, the basis functions can be non-orthogonal
 392 (e.g., $\sum_i \cos[\omega(t_i - t^*)] \sin[\omega(t_i - t^*)] \neq 0$), which can lead to significant errors in esti-
 393 mating the coefficients. To address this, Kirchner and Neal (2013) employ shifted basis
 394 functions such that: $x_i = b_0 + b_1 \cos[\omega(t_i - \tau)] + b_2 \sin[\omega(t_i - \tau)]$, where the time shift
 395 τ is chosen to ensure that the basis functions 1, $\cos[\omega(t_i - \tau)]$, and $\sin[\omega(t_i - \tau)]$ are
 396 mutually orthogonal. The coefficients b_0, b_1 , and b_2 obtained via weighted regression
 397 are then converted back to the original coefficients a_0, a_1 , and a_2 by accounting for
 398 the phase shift $\omega(t^* - \tau)$.

399 The local spectral power, or scalogram, is calculated at each t^* as: $S_{\text{loc}}(t^*, \omega) =$
 400 $\frac{1}{2}(a_1^2 + a_2^2)(t_{\text{max}} - t_{\text{min}}) \frac{n_{\text{eff}}}{n}$, where $t_{\text{max}} - t_{\text{min}}$ is the total time interval covered
 401 by the n samples, and $n_{\text{eff}} = (\sum_i w_i)^2 / \sum_i w_i^2$ represents the effective number of
 402 points. Finally, a robust global estimate of the Power Spectral Density (PSD) is
 403 obtained by averaging the local spectral power over the entire time interval, as
 404 $S(\omega) = \sum_{t^*} v_{\text{eff}}(t^*) S_{\text{loc}}(t^*, \omega) / \sum_{t^*} v_{\text{eff}}(t^*)$, where $v_{\text{eff}}(t^*) = \max\{0, n_{\text{eff}} - 3\}$ is the
 405 effective degrees of freedom [32].

406 The decay constant c determines the frequency resolution in the spectral analysis
 407 and balances the frequency and time resolution in the time-frequency analysis. For
 408 the time-frequency analysis (scalogram), we adopt $c = 1/(8\pi^2)$, the standard value for
 409 this analysis in `Pyleoclim` [33], which provides a balanced resolution for identifying
 410 transient shifts in ice age periodicity. For the global spectral analysis (PSD), we set
 411 $c = 0.0005$. This corresponds to a broader effective time window (slightly smaller than
 412 the default value 0.001 in `Pyleoclim`) to prioritize high frequency resolution.

413 To check the sensitivity of our results, we conduct spectral analyses using multiple
 414 estimators: the conventional periodogram [63] and the Lomb-Scargle periodogram [66,
 415 67]. For the former, the time series is interpolated at 1-kyr intervals. In both cases,

416 the series are linearly detrended over the analysis period. All analyses are performed
417 using the `pyleoclim` (version 1.2.0) [33].

418 Interglacial spacings in Tzedakis et al. (2017)

419 Tzedakis et al. (2017) proposed a simple rule to determine which insolation peaks
420 trigger interglacials [13]. In their model, 51 interglacials are identified over the Qua-
421 ternary based on the LR04 benthic $\delta^{18}\text{O}$ stack [6], supported by additional composite
422 records from Eastern Equatorial Pacific sites. An interglacial onset is defined when the
423 detrended $\delta^{18}\text{O}$ value falls below a lower threshold of 3.68 ‰ after having exceeded a
424 higher threshold of 3.92 ‰. To apply this criterion consistently, $\delta^{18}\text{O}$ values prior to
425 1.5 Ma are detrended as $\delta^{18}\text{O}_{\text{detrended}} = \delta^{18}\text{O} + 3.296 \times 10^{-4}(t - 1500)$, where t is
426 the time in kyr, while values after 1.5 Ma remain unchanged. This trend is attributed
427 to the long-term cooling of deep-water temperatures or an increase in Antarctic ice
428 volume.

429 The T17 model predicts interglacial onsets based on caloric summer half-year
430 insolation. This measure represents the total insolation integrated over the caloric
431 summer half-year, which is defined such that every day within this period receives
432 more insolation than any day in the winter half [11, 12]. At 65°N, the variance of this
433 insolation measure receives approximately equal contributions from climatic preces-
434 sion and obliquity. In the T17 framework, an interglacial is triggered when a peak in
435 the 65°N caloric summer insolation exceeds a threshold that decreases as a function
436 of the time elapsed since the previous interglacial (Δt), reflecting the accumulation
437 of glacial instability. This condition can be expressed as the effective energy, defined
438 as $E(I_{\text{peak}}, \Delta t) = I_{\text{peak}} + b\Delta t$, exceeding a constant deglaciation threshold $I_{\text{threshold}}$.
439 Here, $b = 0.0021 \pm 0.0001 \text{ GJ m}^{-2} \text{ kyr}^{-1}$, and $I_{\text{threshold}}$ is defined to ramp up from
440 6.02 GJ m^{-2} to 6.14 GJ m^{-2} over the interval from 1.55 Ma to 0.61 Ma. Using this
441 criterion, the model can predict most of 51 interglacial onsets, with only two false
442 negatives (MIS 59 and 63). For these false negatives, the insolation peaks immedi-
443 ately preceding their respective isotopic minima are assumed to be the trigger. In the
444 present work, the interglacial spacings (T_{ins}) are defined as the durations between suc-
445 cessive caloric summer insolation peaks that finally induced each interglacial. Using
446 the T17, the interglacial spacing T_{ins} is determined as the minimal peak-to-peak spac-
447 ing that satisfies the condition $E(I_{\text{peak}}, T_{\text{ins}}) = I_{\text{peak}} + bT_{\text{ins}} > T_{\text{threshold}}$. Therefore,
448 $n = \text{argmin}_{\tilde{n} \geq 1} \{I_{\text{peak}} + b(\tilde{n}T_p + \delta) > T_{\text{threshold}}\}$.

449 **Supplementary information.** This article accompanies Supplementary Informa-
450 tion (Supplementary notes, Figures S1–S19, and Table S1).

451 **Acknowledgements.** The author thanks Prof. Polychronis Tzedakis and Prof. Eric
452 W. Wolff for insightful communications that inspired this work.

453 Declarations

- 454 • **Competing interests:** The author declares no competing interests.
- 455 • **Data availability:** The one-to-one correspondence between each glacial cycle
456 and the insolation-based interglacial spacing (Table S1) is provided in

457 Data_S1_formula.xlsx at <https://doi.org/10.5281/zenodo.19534114>. All the other
458 data used in this study are publicly available from the original sources cited in the
459 main text and Supplementary Information.

- 460 • Materials availability: Not applicable.
- 461 • Code availability: Pyleoclim, used for wavelet-based spectral analysis, is available at
462 [clim-util.readthedocs.io/en/latest/">https://pyleoclim-util.readthedocs.io/en/latest/](https://pyleo<span style=) (last accessed 6 April 2026). Other
463 codes used in this study will be uploaded to a repository after the acceptance of the
464 paper.

465 References

- 466 [1] Clark, P. U., Shakun, J. D., Rosenthal, Y., Köhler, P. & Bartlein, P. J. Global
467 and regional temperature change over the past 4.5 million years. *Science* **383**,
468 884–890 (2024).
- 469 [2] Jouzel, J. *et al.* Orbital and millennial antarctic climate variability over the past
470 800,000 years. *science* **317**, 793–796 (2007).
- 471 [3] Rohling, E. J. *et al.* Comparison and synthesis of sea-level and deep-sea tem-
472 perature variations over the past 40 million years. *Reviews of Geophysics* **60**,
473 e2022RG000775 (2022).
- 474 [4] Lüthi, D. *et al.* High-resolution carbon dioxide concentration record 650,000–
475 800,000 years before present. *Nature* **453**, 379–382 (2008).
- 476 [5] Loulergue, L. *et al.* Orbital and millennial-scale features of atmospheric ch4 over
477 the past 800,000 years. *Nature* **453**, 383–386 (2008).
- 478 [6] Lisiecki, L. E. & Raymo, M. E. A pliocene-pleistocene stack of 57 globally
479 distributed benthic $\delta^{18}\text{O}$ records. *Paleoceanography* **20** (2005).
- 480 [7] Herbert, T. D. The mid-pleistocene climate transition. *Annual Review of Earth*
481 *and Planetary Sciences* **51**, 389–418 (2023).
- 482 [8] Berends, C. J., Köhler, P., Lourens, L. J. & van de Wal, R. S. W. On the cause
483 of the mid-pleistocene transition. *Reviews of Geophysics* **59**, e2020RG000727
484 (2021). E2020RG000727 2020RG000727.
- 485 [9] McClymont, E. L., Sostdian, S. M., Rosell-Melé, A. & Rosenthal, Y. Pleistocene
486 sea-surface temperature evolution: Early cooling, delayed glacial intensifica-
487 tion, and implications for the mid-pleistocene climate transition. *Earth-Science*
488 *Reviews* **123**, 173–193 (2013).
- 489 [10] Laskar, J. *et al.* A long-term numerical solution for the insolation quantities of
490 the earth. *Astronomy & Astrophysics* **428**, 261–285 (2004).

- 491 [11] Milankovitch, M. Kanon der erdbestahlung und seine anwendung auf das
492 eiszeitproblem, 133. *Königlich Serbische Academie, Belgrade* (1941).
- 493 [12] Crucifix, M. Palinsol: insolation for palaeoclimate studies, r package version 0.93
494 (2016).
- 495 [13] Tzedakis, P., Crucifix, M., Mitsui, T. & Wolff, E. W. A simple rule to determine
496 which insolation cycles lead to interglacials. *Nature* **542**, 427–432 (2017).
- 497 [14] Paillard, D. Glacial cycles: toward a new paradigm. *Reviews of Geophysics* **39**,
498 325–346 (2001).
- 499 [15] Hays, J. D., Imbrie, J. & Shackleton, N. J. Variations in the earth’s orbit:
500 Pacemaker of the ice ages. *Science* **194**, 1121–1132 (1976).
- 501 [16] Berger, A. Support for the astronomical theory of climatic change. *Nature* **269**,
502 44–45 (1977).
- 503 [17] Raymo, M. The timing of major climate terminations. *Paleoceanography* **12**,
504 577–585 (1997).
- 505 [18] Ridgwell, A. J., Watson, A. J. & Raymo, M. E. Is the spectral signature of the
506 100 kyr glacial cycle consistent with a milankovitch origin? *Paleoceanography* **14**,
507 437–440 (1999).
- 508 [19] Blackburn, T., Kodama, S. & Piccione, G. Eccentricity paces late pleistocene
509 glaciations. *Geophysical Research Letters* **51**, e2024GL108751 (2024).
- 510 [20] Huybers, P. & Wunsch, C. Obliquity pacing of the late pleistocene glacial
511 terminations. *Nature* **434**, 491–494 (2005).
- 512 [21] Nyman, K. H. & Ditlevsen, P. D. The middle pleistocene transition by frequency
513 locking and slow ramping of internal period. *Climate Dynamics* **53**, 3023–3038
514 (2019).
- 515 [22] Bajo, P. *et al.* Persistent influence of obliquity on ice age terminations since the
516 middle pleistocene transition. *Science* **367**, 1235–1239 (2020).
- 517 [23] Abe-Ouchi, A. *et al.* Insolation-driven 100,000-year glacial cycles and hysteresis
518 of ice-sheet volume. *Nature* **500**, 190–193 (2013).
- 519 [24] Cheng, H. *et al.* The asian monsoon over the past 640,000 years and ice age
520 terminations. *nature* **534**, 640–646 (2016).
- 521 [25] Barker, S. *et al.* Persistent influence of precession on northern ice sheet variability
522 since the early pleistocene. *Science* **376**, 961–967 (2022).

- 523 [26] Hobart, B., Lisiecki, L. E., Rand, D., Lee, T. & Lawrence, C. E. Late pleistocene
524 100-kyr glacial cycles paced by precession forcing of summer insolation. *Nature*
525 *Geoscience* **16**, 717–722 (2023).
- 526 [27] Huybers, P. Combined obliquity and precession pacing of late pleistocene
527 deglaciations. *Nature* **480**, 229–232 (2011).
- 528 [28] Mitsui, T., Willeit, M. & Boers, N. Synchronization phenomena observed in
529 glacial-interglacial cycles simulated in an earth system model of intermediate
530 complexity. *Earth System Dynamics* **2023**, 1277–1294 (2023). URL <https://doi.org/10.5194/esd-14-1277-2023>.
531
- 532 [29] Mitsui, T., Tzedakis, P. C. & Wolff, E. W. Insolation evolution and ice volume
533 legacies determine interglacial and glacial intensity. *Climate of the Past* **18**,
534 1983–1996 (2022).
- 535 [30] Barker, S., Lisiecki, L. E., Knorr, G., Nuber, S. & Tzedakis, P. C. Distinct roles
536 for precession, obliquity, and eccentricity in pleistocene 100-kyr glacial cycles.
537 *Science* **387**, eadp3491 (2025).
- 538 [31] Foster, G. Time series analysis by projection. i. statistical properties of fourier
539 analysis. *Astronomical Journal v. 111, p. 541* **111**, 541 (1996).
- 540 [32] Kirchner, J. W. & Neal, C. Universal fractal scaling in stream chemistry and its
541 implications for solute transport and water quality trend detection. *Proceedings*
542 *of the National Academy of Sciences* **110**, 12213–12218 (2013).
- 543 [33] Khider, D. *et al.* Pyleoclim: Paleoclimate timeseries analysis and visualization
544 with python. *Paleoceanography and Paleoclimatology* **37**, e2022PA004509 (2022).
- 545 [34] Lisiecki, L. A benthic $\delta^{13}\text{C}$ -based proxy for atmospheric pCO_2 over the last 1.5
546 myr. *Geophysical Research Letters* **37** (2010).
- 547 [35] Zhou, Y., Lisiecki, L. E., Meyers, S. R., Lee, T. & Lawrence, C. Global and
548 regional pleistocene benthic $\delta^{18}\text{O}$ stacks with a comparison of different age
549 modeling strategies. *Geochronology* **8**, 85–107 (2026).
- 550 [36] Meyers, S. R. The evaluation of eccentricity-related amplitude modulation and
551 bundling in paleoclimate data: An inverse approach for astrochronologic testing
552 and time scale optimization. *Paleoceanography* **30**, 1625–1640 (2015).
- 553 [37] Huybers, P. Glacial variability over the last two million years: an extended depth-
554 derived age model, continuous obliquity pacing, and the pleistocene progression.
555 *Quaternary Science Reviews* **26**, 37–55 (2007).
- 556 [38] Mudelsee, M. & Stattegger, K. Exploring the structure of the mid-pleistocene
557 revolution with advanced methods of time-series analysis. *Geologische Rundschau*

- 558 **86**, 499–511 (1997).
- 559 [39] Clark, P. U. *et al.* The middle pleistocene transition: characteristics, mechanisms,
560 and implications for long-term changes in atmospheric pco₂. *Quaternary Science*
561 *Reviews* **25**, 3150–3184 (2006).
- 562 [40] Lisiecki, L. E. & Raymo, M. E. Plio–pleistocene climate evolution: trends and
563 transitions in glacial cycle dynamics. *Quaternary Science Reviews* **26**, 56–69
564 (2007).
- 565 [41] Huybers, P. & Wunsch, C. A depth-derived pleistocene age model: Uncertainty
566 estimates, sedimentation variability, and nonlinear climate change. *Paleoceanog-*
567 *raphy* **19** (2004).
- 568 [42] Huybers, P. & Aharonson, O. Orbital tuning, eccentricity, and the frequency
569 modulation of climatic precession. *Paleoceanography* **25** (2010).
- 570 [43] Liautaud, P. R., Hodell, D. A. & Huybers, P. J. Detection of significant climatic
571 precession variability in early pleistocene glacial cycles. *Earth and Planetary*
572 *Science Letters* **536**, 116137 (2020).
- 573 [44] Watanabe, Y. *et al.* Astronomical forcing shaped the timing of early pleistocene
574 glacial cycles. *Communications Earth & Environment* **4** (2023).
- 575 [45] Liebrand, D. & de Bakker, A. Bispectra of climate cycles show how ice ages are
576 fuelled. *Climate of the Past* **15**, 1959–1983 (2019).
- 577 [46] Bolton, E. W., Maasch, K. A. & Lilly, J. M. A wavelet analysis of plio-pleistocene
578 climate indicators: A new view of periodicity evolution. *Geophysical Research*
579 *Letters* **22**, 2753–2756 (1995).
- 580 [47] Rial, J. A. Pacemaking the ice ages by frequency modulation of earth’s orbital
581 eccentricity. *Science* **285**, 564–568 (1999).
- 582 [48] Cheng, H. *et al.* Ice age terminations. *Science* **326**, 248–252 (2009).
- 583 [49] Raymo, M. E. & Nisancioglu, K. H. The 41 kyr world: Milankovitch’s other
584 unsolved mystery. *Paleoceanography* **18** (2003).
- 585 [50] Legrain, E., Parrenin, F. & Capron, E. A gradual change is more likely to have
586 caused the mid-pleistocene transition than an abrupt event. *Communications*
587 *Earth & Environment* **4**, 90 (2023).
- 588 [51] Kodama, S. T. & Blackburn, T. Eccentricity controls the magnitude and peri-
589 odicity of pleistocene glacial cycles. *Paleoceanography and Paleoclimatology* **41**,
590 e2026PA005420 (2026).

- 591 [52] Hönisch, B., Hemming, N. G., Archer, D., Siddall, M. & McManus, J. F.
592 Atmospheric carbon dioxide concentration across the mid-pleistocene transition.
593 *Science* **324**, 1551–1554 (2009).
- 594 [53] Chalk, T. B. *et al.* Causes of ice age intensification across the mid-pleistocene
595 transition. *Proceedings of the National Academy of Sciences* **114**, 13114–13119
596 (2017).
- 597 [54] Willeit, M., Ganopolski, A., Calov, R. & Brovkin, V. Mid-pleistocene transition in
598 glacial cycles explained by declining co2 and regolith removal. *Science Advances*
599 **5**, eaav7337 (2019).
- 600 [55] Yehudai, M. *et al.* Evidence for a northern hemispheric trigger of the 100,000-
601 y glacial cyclicity. *Proceedings of the National Academy of Sciences* **118**,
602 e2020260118 (2021).
- 603 [56] Clark, P. U. & Pollard, D. Origin of the middle pleistocene transition by ice sheet
604 erosion of regolith. *Paleoceanography* **13**, 1–9 (1998).
- 605 [57] An, Z. *et al.* Mid-pleistocene climate transition triggered by antarctic ice sheet
606 growth. *science* **385**, 560–565 (2024).
- 607 [58] Basak, C. *et al.* Southern hemisphere initiation of the mid-pleistocene transition.
608 *Science Advances* **12**, eaea6811 (2026).
- 609 [59] Hines, S. K. *et al.* Revisiting the mid-pleistocene transition ocean circulation
610 crisis. *Science* **386**, 681–686 (2024).
- 611 [60] Mitsui, T., Ditlevsen, P., Boers, N. & Crucifix, M. 100 kyr ice age cycles as a
612 timescale-matching problem. *Earth System Dynamics* **16**, 1569–1584 (2025).
- 613 [61] Lisiecki, L. E. Links between eccentricity forcing and the 100,000-year glacial
614 cycle. *Nature geoscience* **3**, 349–352 (2010).
- 615 [62] Meyers, S. R. Cyclostratigraphy and the problem of astrochronologic testing.
616 *Earth-Science Reviews* **190**, 190–223 (2019).
- 617 [63] Bloomfield, P. *Fourier analysis of time series: an introduction* (John Wiley &
618 Sons, 2004).
- 619 [64] Thomson, D. J. Spectrum estimation and harmonic analysis. *Proceedings of the*
620 *IEEE* **70**, 1055–1096 (1982).
- 621 [65] Schulz, M. & Mudelsee, M. Redfit: estimating red-noise spectra directly from
622 unevenly spaced paleoclimatic time series. *Computers & Geosciences* **28**, 421–426
623 (2002).

- 624 [66] Lomb, N. R. Least-squares frequency analysis of unequally spaced data.
625 *Astrophysics and space science* **39**, 447–462 (1976).
- 626 [67] Scargle, J. D. Studies in astronomical time series analysis. ii-statistical aspects
627 of spectral analysis of unevenly spaced data. *Astrophysical Journal, Part 1, vol.*
628 *263, Dec. 15, 1982, p. 835-853.* **263**, 835–853 (1982).
- 629 [68] Wu, Z., Huang, N. E., Long, S. R. & Peng, C.-K. On the trend, detrending, and
630 variability of nonlinear and nonstationary time series. *Proceedings of the National*
631 *Academy of Sciences* **104**, 14889–14894 (2007).
- 632 [69] Zhu, F. *et al.* Climate models can correctly simulate the continuum of global-
633 average temperature variability. *Proceedings of the National Academy of Sciences*
634 **116**, 8728–8733 (2019).

1 Supplementary Information for Beyond the
2 100-kyr and 41-kyr dichotomy: ~ 76 - and ~ 52 -kyr
3 signals and forbidden periodicities in Quaternary
4 glacial cycles

5 Takahito Mitsui

6 Faculty of Health Data Science, Juntendo University, Urayasu, Chiba,
7 279-0013, Japan.

8
9 Contact: takahito321@gmail.com.

10 **Contents**

- 11 • Supplementary Notes
12 • References
13 • Supplementary Figures S1–S18
14 • Supplementary Table S1, which is also available as
15 Data_S1_formula.xlsx at <https://doi.org/10.5281/zenodo.19534114>

16 **Derivation of the approximation formulae of**
17 **interglacial spacings**

18 Following Tzedakis et al. (2017) [1], we assume that each interglacial onset can be
19 linked with a specific peak in the caloric summer half-year insolation at 65°N [2, 3].
20 Thus, the insolation-based interglacial spacings (T_{ins}) are defined between successive
21 caloric summer half-year insolation peaks that finally induced each interglacial [1]
22 (Figs. S11a–S13a). Here we derive approximate formulae for T_{ins} of each glacial cycle
23 based on local information on climatic precession and obliquity [4] (Fig. S15–S18).

24 It is known that the caloric summer half-year insolation, especially at 65°N , is well
25 approximated by a superposition of standardized indices of climatic precession and
26 obliquity [2, 5]. Since the climatic precession oscillates more rapidly than obliquity, the

27 insolation peak closest to the deglaciation isotopic change is more tightly linked with
 28 a climatic precession peak (minimum). Indeed, the link between the length of glacial
 29 cycles and the durations of astronomical cycles—particularly precession—has been
 30 noted in various studies [6–9]. On the other hand, the duration of climatic precession
 31 cycles varies widely (between 14 and 31 kyr) when eccentricity is low, whereas it
 32 remains relatively stable around 22.1 kyr when eccentricity is high (Fig. S14) [9, 10].
 33 Building on this, we here derive finer relationships between T_{ins} and the evolving
 34 durations of precession and obliquity cycles.

35 For each glacial cycle, we approximate the local variations in the caloric summer
 36 half-year insolation as $f(t) = A_p \cos(\omega_p t + \varphi_p) + A_o \cos(\omega_o t + \varphi_o)$, accounting for the
 37 respective positive contributions of climatic precession and obliquity to the insolation.
 38 Here, $A_{p,o}$ are the local-mean amplitudes, $\omega_{p,o}$ are the angular frequencies (correspond-
 39 ing to local-mean periods $T_{p,o}$), and $\varphi_{p,o}$ are the local phases of climatic precession and
 40 obliquity cycles. Note that the maxima of $A_p \cos(\omega_p t + \varphi_p)$ correspond to the minima
 41 of the climatic precession cycles, as precession minima contribute to maximal insolation.
 42 Then, we can derive analytical expressions for T_{ins} . A complete correspondence
 43 between individual glacial cycles and their respective formulae is provided in Table S1.

Formula type 2a, 3a, 4a and 5a. When the peaks of climatic precession and
 obliquity nearly coincide and collectively induce an interglacial, we define this peak
 time as $t = 0$ by setting $\varphi_p = \varphi_o = 0$ (Fig. S19a). If the spacing T_{ins} between the peak
 at $t = 0$ and a subsequent interglacial-inducing peak is close to the n -th multiple of the
 local-mean precession period T_p , it can be expressed as $T_{\text{ins}} = nT_p + \delta$, where the small
 shift δ reflects the phase modulation by obliquity. By linearizing the peak condition
 $f'(nT_p + \delta) = 0$ as $f'(nT_p + \delta) \approx f'(nT_p) + f''(nT_p)\delta = 0$, we obtain approximation
 formulae for T_{ins} ($n = 2, 3, 4, 5$), called type-a:

$$T_{\text{ins}} \approx nT_p - \frac{A_o \omega_o \sin(n\omega_o T_p)}{A_p \omega_p^2 + A_o \omega_o^2 \cos(n\omega_o T_p)}.$$

44 An example of type-a is the ~ 76 -kyr spacing between interglacials MIS 11c and MIS 9e
 45 (Fig. S15), where the corresponding insolation peaks are separated by approximately
 46 four precession cycles ($n = 4$), and the local-mean precession period is $T_p = 18.25$ kyr.
 47 Furthermore, the local-mean obliquity period is $T_o = 41.5$ kyr. The type-a formula
 48 then predicts $T_{\text{ins}} = 74.3$ kyr. This value is closer to the actual value of 76 kyr than the
 49 simple multiple of precession, $nT_p = 73$ kyr, obtained without the shift $\delta = 1.43$ kyr.

Formulae type 1b and 3b. The second case occurs when a glacial cycle spans
 roughly one or three precession cycles (i.e., $n = 1$ or 3), with the insolation locally
 approximated as $f(t) = -A_p \cos(\omega_p t) - A_o \cos(\omega_o t)$ over the interval $-\frac{n}{2}T_p \lesssim t \lesssim \frac{n}{2}T_p$
 (corresponding to $\varphi_p = \varphi_o = \pi$). For this case, we assume that deglaciations occur at
 $t = \pm(\frac{n}{2}T_p + \delta)$, with δ being a small obliquity-induced shift. By linearizing the peak
 condition $f'(\frac{n}{2}T_p + \delta) \approx f'(\frac{n}{2}T_p) + f''(\frac{n}{2}T_p)\delta = 0$, we obtain approximation formulae
 for T_{ins} ($n = 1, 3$), called type-1b or 3b:

$$T_{\text{ins}} \approx nT_p + \frac{2A_o \omega_o \sin(\frac{n}{2}\omega_o T_p)}{A_p \omega_p^2 - A_o \omega_o^2 \cos(\frac{n}{2}\omega_o T_p)}.$$

50 An example of type-3b is the spacing between interglacials MIS 37 and MIS 35
 51 (Fig. S16). The corresponding insolation peaks are separated by approximately three
 52 precession cycles ($n = 3$), and the local-mean precession period is $T_p = 19$ kyr. Fur-
 53 thermore, the local-mean obliquity period is $T_o = 39$ kyr. Then, the type-3b formula
 54 predicts $T_{\text{ins}} = 54.2$ kyr. This value is closer to the actual value of 53 kyr than the
 55 simple multiple of precession, $nT_p = 57$ kyr, obtained without the shift $\delta = -2.8$ kyr.

Formulae type 2b. Consider a case where a glacial cycle spans approximately two precession cycles, in which the central precession peak is counteracted by an obliquity minimum, while the outer precession peaks are enhanced by adjacent obliquity maxima. This situation is approximated as $f(t) = A_p \cos(\omega_p t) - A_o \cos(\omega_o t)$ over the interval $-T_p \lesssim t \lesssim T_p$ (corresponding to $\varphi_p = 0$ and $\varphi_o = \pi$). In a similar manner to the derivation of the formulae type-1b and 3b, T_{ins} is given by formula called type-2b:

$$T_{\text{ins}} \approx 2T_p + \frac{2A_o\omega_o \sin(\omega_o T_p)}{A_p\omega_p^2 - A_o\omega_o^2 \cos(\omega_o T_p)}.$$

Formulae type 4b. Consider a case where a glacial cycle spans approximately four precession cycles, in which the central precession peak is enhanced by an obliquity maximum, while the outer precession peaks are also enhanced by adjacent obliquity maxima. This situation is approximated as $f(t) = A_p \cos(\omega_p t) + A_o \cos(\omega_o t)$ over the interval $-2T_p \lesssim t \lesssim 2T_p$ (corresponding to $\varphi_p = \varphi_o = 0$). In a similar manner to the derivation of the formulae type-2b, T_{ins} is given by formula called type-4b:

$$T_{\text{ins}} \approx 4T_p - \frac{2A_o\omega_o \sin(2\omega_o T_p)}{A_p\omega_p^2 + A_o\omega_o^2 \cos(2\omega_o T_p)}.$$

Formulae type 1c and 2c. Consider a case where a glacial cycle spans roughly one or two precession cycles ($n = 1$ or 2), with the insolation locally approximated as $f(t) = A_p \cos(\omega_p t) - A_o \sin(\omega_o t)$ over the interval $0 \leq t \lesssim nT_p$ (corresponding to $\varphi_p = 0$ and $\varphi_o = \frac{\pi}{2}$). In this case, the deglaciations occur at $t = 0$ and $t = nT_p + \delta$, where δ is a small shift. By linearizing the peak condition $f'(nT_p + \delta) \approx f'(nT_p) + f''(nT_p)\delta = 0$, we obtain approximation formulae for T_{ins} ($n = 1, 2$), called type-1c or 2c:

$$T_{\text{ins}} \approx nT_p - \frac{A_o\omega_o \cos(n\omega_o T_p)}{A_p\omega_p^2 - A_o\omega_o^2 \sin(n\omega_o T_p)}.$$

Formula 2d. Consider a case where a glacial cycle spans roughly two precession cycles, with the insolation locally approximated as $f(t) = A_p \cos(\omega_p t) + A_o \sin(\omega_o t)$ over the interval $0 \leq t \lesssim 2T_p$ (corresponding to $\varphi_p = 0$ and $\varphi_o = -\frac{\pi}{2}$). In this case, the deglaciations occur at $t = 0$ and $t = 2T_p + \delta$, where δ is a small shift. By linearizing the peak condition $f'(2T_p + \delta) \approx f'(2T_p) + f''(2T_p)\delta = 0$, we obtain the approximation formula for T_{ins} , called type-2d:

$$T_{\text{ins}} \approx 2T_p + \frac{A_o\omega_o \cos(2\omega_o T_p)}{A_p\omega_p^2 - A_o\omega_o^2 \sin(2\omega_o T_p)}.$$

Formula type pp. In this case, the interglacial spacing is primarily determined by the spacing between precession peaks; while obliquity cycles may shift the timing of both deglaciations, they do so by the same amount, leaving the net spacing almost unchanged. Therefore,

$$T_{\text{ins}} \approx nT_p.$$

56 **Choice of amplitude $A_{p,o}$.** Climatic precession and obliquity contribute nearly
57 equally to the total variance in the caloric summer half-year insolation at 65°N [2, 3].
58 Therefore, for simplicity, we set $A_{p,o} = 1$ for 65°N caloric summer half-year insolation
59 except for the following two cycles. However, the cycle from MIS 99 to 97 as well as
60 the cycle from MIS 97 to 95 are characterized by low eccentricity (i.e., low precession
61 amplitude) and high obliquity amplitude. Assessing their variances locally, we took
62 $A_o/A_p = 3$ and $A_o/A_p = 2.5$ for the former and the latter, respectively.

63 **Two exceptions** The spacings MIS 95–93 and MIS 93–91 represent epochs during
64 which eccentricity remains near zero. The aforementioned formulae are inapplicable to
65 these events because deglaciation coincides with the obliquity maximum at 2386 ka,
66 where eccentricity is virtually zero. For these cases, we adopt simplified estimates for
67 T_{ins} . The MIS 95–93 interval is assumed to be initiated by an insolation peak occurring
68 midway between the obliquity maximum at 2426 ka and the precession minimum at
69 2419 ka, and is finalized by the obliquity maximum at 2386 ka. Consequently, the
70 spacing is estimated as $(2426 + 2419)/2 - 2386 = 36.5$ kyr. Similarly, the MIS 93–91
71 interval is initiated by the 2386-ka obliquity maximum and finalized by an insolation
72 peak midway between the obliquity maximum at 2348 ka and the precession minimum
73 at 2347 ka. The spacing is thus estimated as $2386 - (2348 + 2347)/2 = 38.5$ kyr.

74 References

- 75 [1] Tzedakis, P., Crucifix, M., Mitsui, T. & Wolff, E. W. A simple rule to determine
76 which insolation cycles lead to interglacials. *Nature* **542**, 427–432 (2017).
- 77 [2] Milankovitch, M. Kanon der erdbestahlung und seine anwendung auf das
78 eiszeitproblem, 133. *Königlich Serbische Academie, Belgrade* (1941).
- 79 [3] Crucifix, M. Palinsol: insolation for palaeoclimate studies, r package version 0.93
80 (2016).
- 81 [4] Laskar, J. *et al.* A long-term numerical solution for the insolation quantities of
82 the earth. *Astronomy & Astrophysics* **428**, 261–285 (2004).
- 83 [5] Nisancioglu, K. H. Plio-pleistocene glacial cycles and milankovitch variability.
84 *Elements of Physical Oceanography: A derivative of the Encyclopedia of Ocean*
85 *Sciences* 344 (2009).
- 86 [6] Abe-Ouchi, A. *et al.* Insolation-driven 100,000-year glacial cycles and hysteresis
87 of ice-sheet volume. *Nature* **500**, 190–193 (2013).

- 88 [7] Cheng, H. *et al.* The asian monsoon over the past 640,000 years and ice age
89 terminations. *nature* **534**, 640–646 (2016).
- 90 [8] Hobart, B., Lisiecki, L. E., Rand, D., Lee, T. & Lawrence, C. E. Late pleistocene
91 100-kyr glacial cycles paced by precession forcing of summer insolation. *Nature*
92 *Geoscience* **16**, 717–722 (2023).
- 93 [9] Blackburn, T., Kodama, S. & Piccione, G. Eccentricity paces late pleistocene
94 glaciations. *Geophysical Research Letters* **51**, e2024GL108751 (2024).
- 95 [10] Huybers, P. & Aharonson, O. Orbital tuning, eccentricity, and the frequency
96 modulation of climatic precession. *Paleoceanography* **25** (2010).
- 97 [11] Lisiecki, L. E. & Raymo, M. E. A pliocene-pleistocene stack of 57 globally
98 distributed benthic $\delta^{18}\text{O}$ records. *Paleoceanography* **20** (2005).
- 99 [12] Lisiecki, L. A benthic $\delta^{13}\text{C}$ -based proxy for atmospheric pCO_2 over the last 1.5
100 myr. *Geophysical Research Letters* **37** (2010).
- 101 [13] Zhou, Y., Lisiecki, L. E., Meyers, S. R., Lee, T. & Lawrence, C. Global and
102 regional pleistocene benthic $\delta^{18}\text{O}$ stacks with a comparison of different age
103 modeling strategies. *Geochronology* **8**, 85–107 (2026).
- 104 [14] Meyers, S. R. The evaluation of eccentricity-related amplitude modulation and
105 bundling in paleoclimate data: An inverse approach for astrochronologic testing
106 and time scale optimization. *Paleoceanography* **30**, 1625–1640 (2015).
- 107 [15] Meyers, S. R. Cyclostratigraphy and the problem of astrochronologic testing.
108 *Earth-Science Reviews* **190**, 190–223 (2019).
- 109 [16] Huybers, P. Glacial variability over the last two million years: an extended depth-
110 derived agetmodel, continuous obliquity pacing, and the pleistocene progression.
111 *Quaternary Science Reviews* **26**, 37–55 (2007).
- 112 [17] Barker, S. *et al.* Persistent influence of precession on northern ice sheet variability
113 since the early pleistocene. *Science* **376**, 961–967 (2022).
- 114 [18] Khider, D. *et al.* Pyleoclim: Paleoclimate timeseries analysis and visualization
115 with python. *Paleoceanography and Paleoclimatology* **37**, e2022PA004509 (2022).

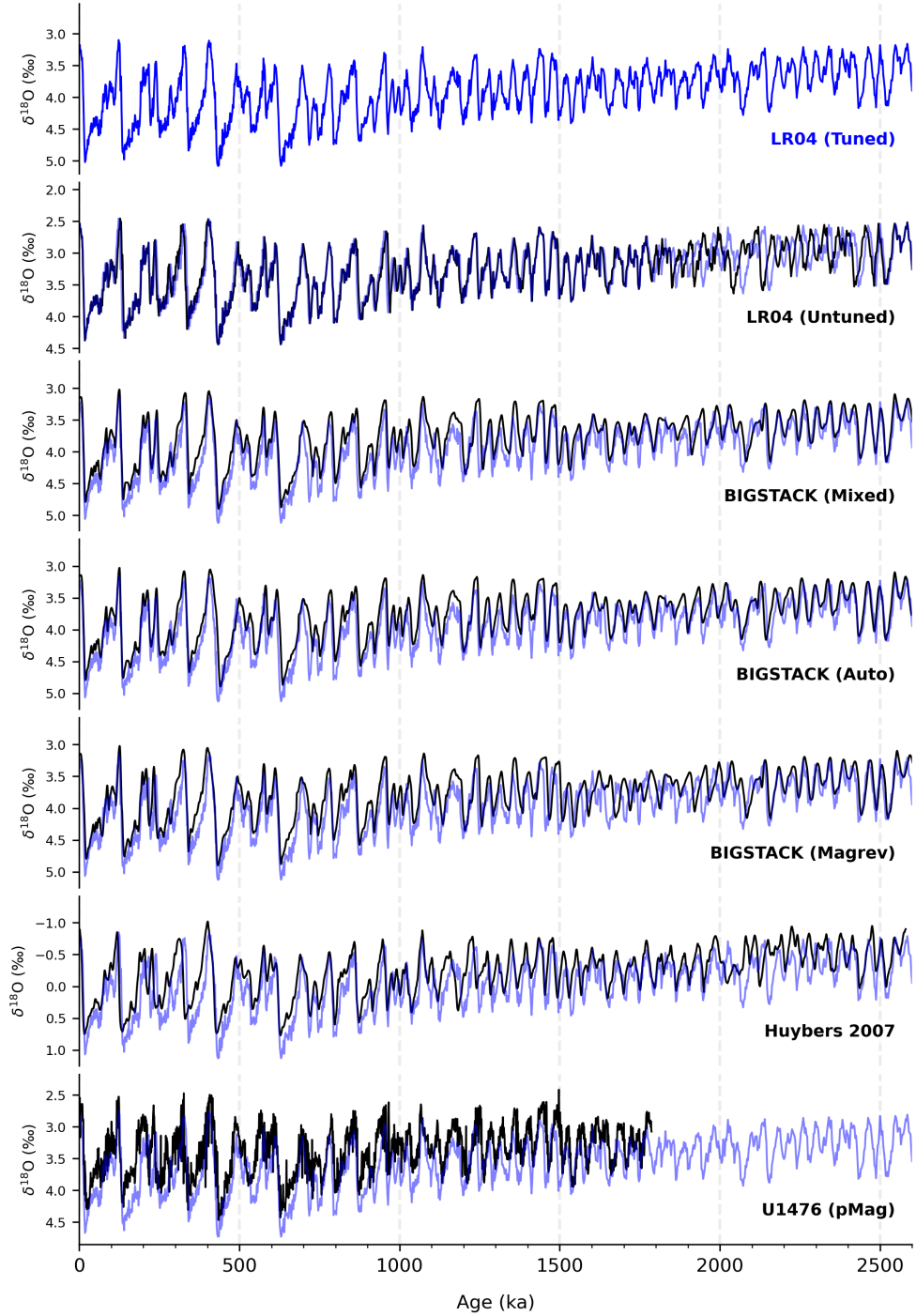


Fig. S1 Benthic $\delta^{18}\text{O}$ stacks and an individual record analyzed in this study. (a) The LR04 tuned stack [11]. In the subsequent panels, the LR04 stack is shown as a blue background reference, vertically shifted to match the mean $\delta^{18}\text{O}$ value of each target record (black). (b) The tuning-free version of the LR04 stack from Lisiecki (2010) [12]. (c) The $\text{BIGSTACK}_{\text{mixed}}$ record using speleothem-based age constraints for 0–654 ka and ice-sheet model tuning for earlier intervals [13]. (d) The $\text{BIGSTACK}_{\text{auto}}$ record obtained from $\text{BIGSTACK}_{\text{magrev}}$ (below) by applying the eTimeOpt algorithm [14, 15] to minimally tune the pervasive 41-kyr obliquity signal. (e) The $\text{BIGSTACK}_{\text{magrev}}$ record constrained by paleomagnetic events over the last 2.606 Ma to minimize orbital circularity. (f) The depth-derived stack of Huybers (2007) [16]. (g) The single-site benthic $\delta^{18}\text{O}$ record from IODP Site U1476, anchored to an independent paleomagnetic age model (U1476pMag) [17]. This record spans only the last 1786.542 kyr.

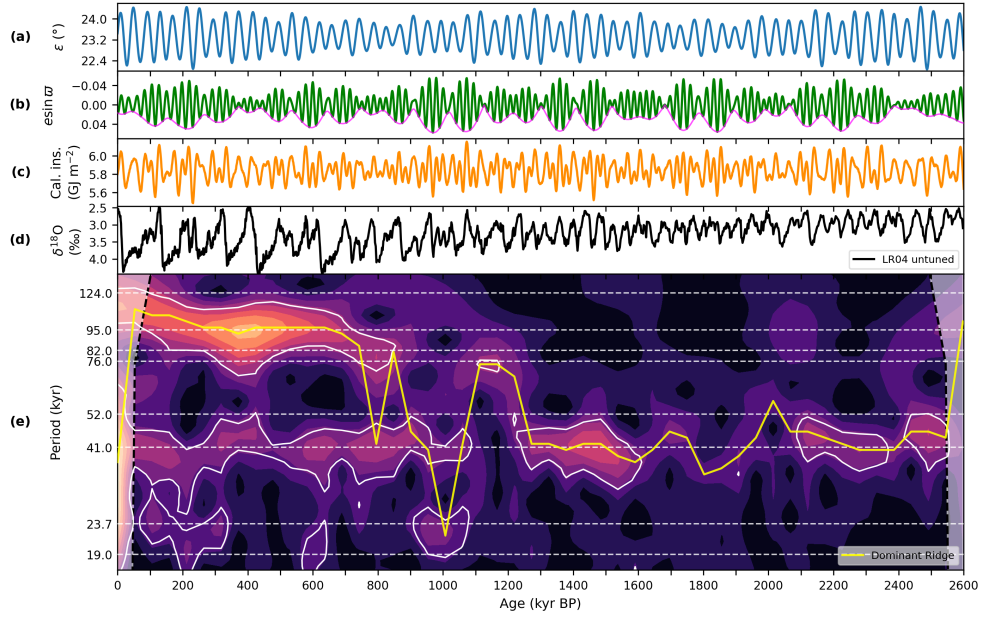


Fig. S2 Time-series and wavelet analyses of the LR04 benthic $\delta^{18}\text{O}$ stack record free from orbital tuning [12], aligned with astronomical forcing [4] over the last 2.6 Myr. (a) Obliquity (ϵ). (b) Climatic precession ($e \sin \varpi$, green) shown with its eccentricity envelope (e , magenta). (c) Caloric summer half-year insolation at 65°N [2, 3]. (d) LR04 benthic $\delta^{18}\text{O}$ stack record without orbital tuning. [12] (e) Wavelet power scalogram of the $\delta^{18}\text{O}$ record. The yellow line indicates the ridge of maximum wavelet power. Areas enclosed by white dashed lines indicate power significant at the 95% confidence level against an AR(1) benchmark. Horizontal dashed lines denote major astronomical periodicities, including the 76-kyr and 52-kyr scales discussed in this study.

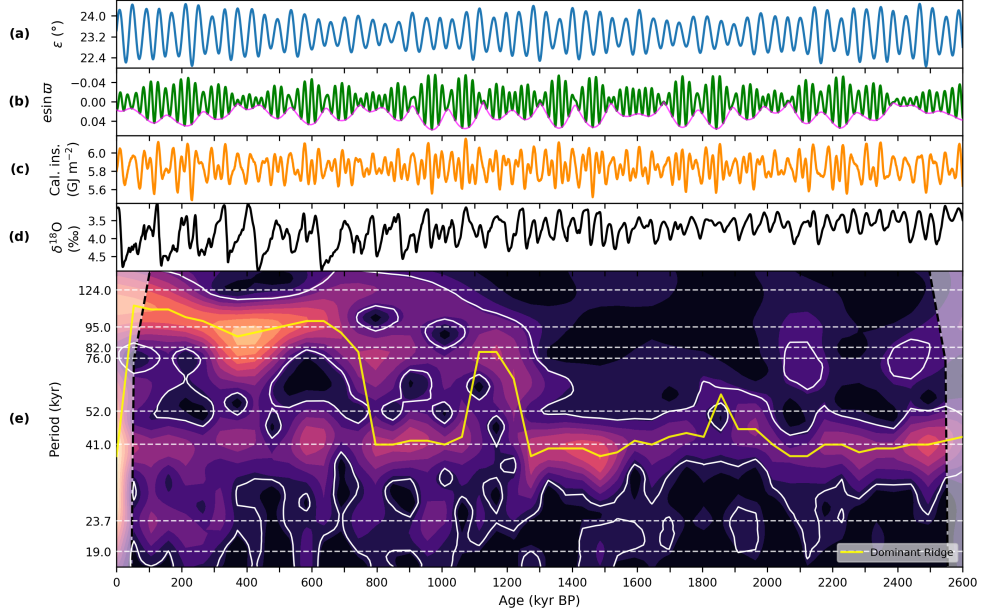


Fig. S3 Time-series and wavelet analyses of the benthic $\delta^{18}\text{O}$ stack record of $\text{BIGSTACK}_{\text{mixed}}$ [13], aligned with astronomical forcing [4] over the last 2.6 Myr. (a) Obliquity (ϵ). (b) Climatic precession ($e \sin \varpi$, green) shown with its eccentricity envelope (e , magenta). (c) Caloric summer half-year insolation at 65°N [2, 3]. (d) The benthic $\delta^{18}\text{O}$ stack record of Huybers (2007) [16]. (e) Wavelet power scalogram of the $\delta^{18}\text{O}$ record. The yellow line indicates the ridge of maximum wavelet power. Areas enclosed by white dashed lines indicate power significant at the 95% confidence level against an AR(1) benchmark. Horizontal dashed lines denote major astronomical periodicities, including the 76-kyr and 52-kyr scales discussed in this study.

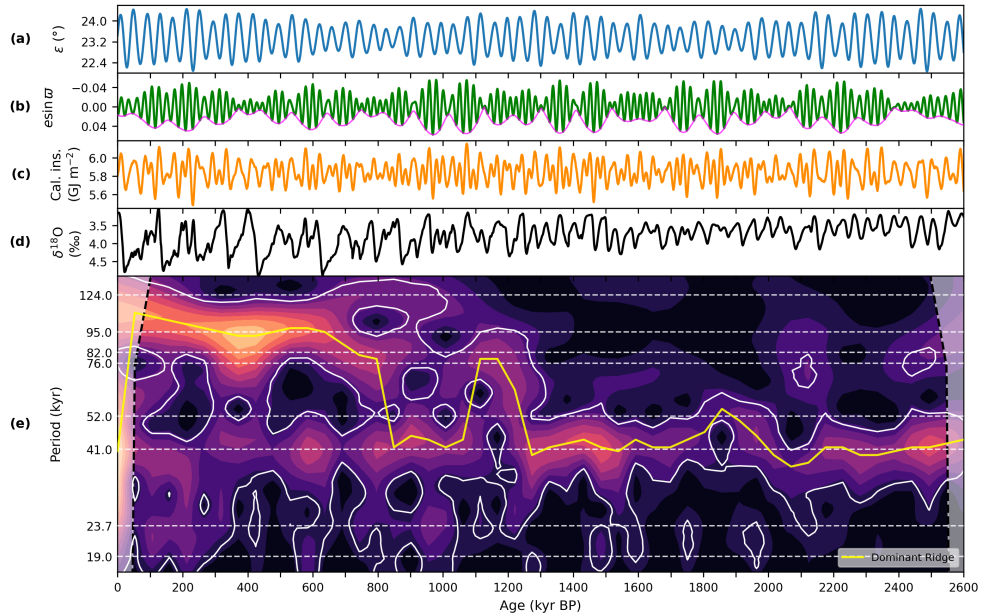


Fig. S4 Time-series and wavelet analyses of the benthic $\delta^{18}\text{O}$ stack record of BIGSTACK_{magrev} [13], aligned with astronomical forcing [4] over the last 2.6 Myr. (a) Obliquity (ϵ). (b) Climatic precession ($e \sin \omega$, green) shown with its eccentricity envelope (e , magenta). (c) Caloric summer half-year insolation at 65°N [2, 3]. (d) The benthic $\delta^{18}\text{O}$ stack record of Huybers (2007) [16]. (e) Wavelet power scalogram of the $\delta^{18}\text{O}$ record. The yellow line indicates the ridge of maximum wavelet power. Areas enclosed by white dashed lines indicate power significant at the 95% confidence level against an AR(1) benchmark. Horizontal dashed lines denote major astronomical periodicities, including the 76-kyr and 52-kyr scales discussed in this study.

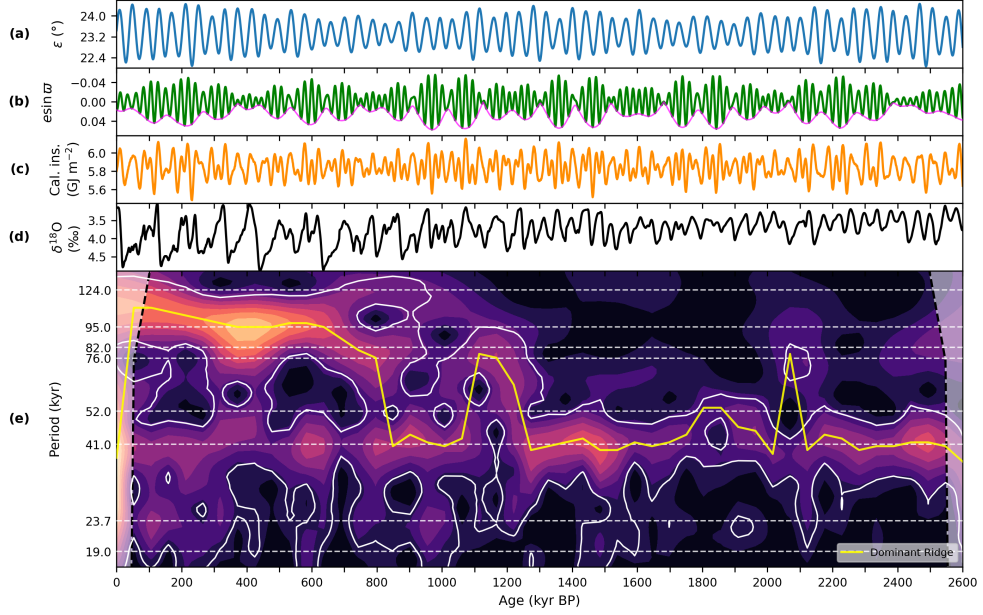


Fig. S5 Time-series and wavelet analyses of the benthic $\delta^{18}\text{O}$ stack record of $\text{BIGSTACK}_{\text{auto}}$ [13], aligned with astronomical forcing [4] over the last 2.6 Myr. (a) Obliquity (ϵ). (b) Climatic precession ($e \sin \omega$, green) shown with its eccentricity envelope (e , magenta). (c) Caloric summer half-year insolation at 65°N [2, 3]. (d) The benthic $\delta^{18}\text{O}$ stack record of Huybers (2007) [16]. (e) Wavelet power scalogram of the $\delta^{18}\text{O}$ record. The yellow line indicates the ridge of maximum wavelet power. Areas enclosed by white dashed lines indicate power significant at the 95% confidence level against an AR(1) benchmark. Horizontal dashed lines denote major astronomical periodicities, including the 76-kyr and 52-kyr scales discussed in this study.

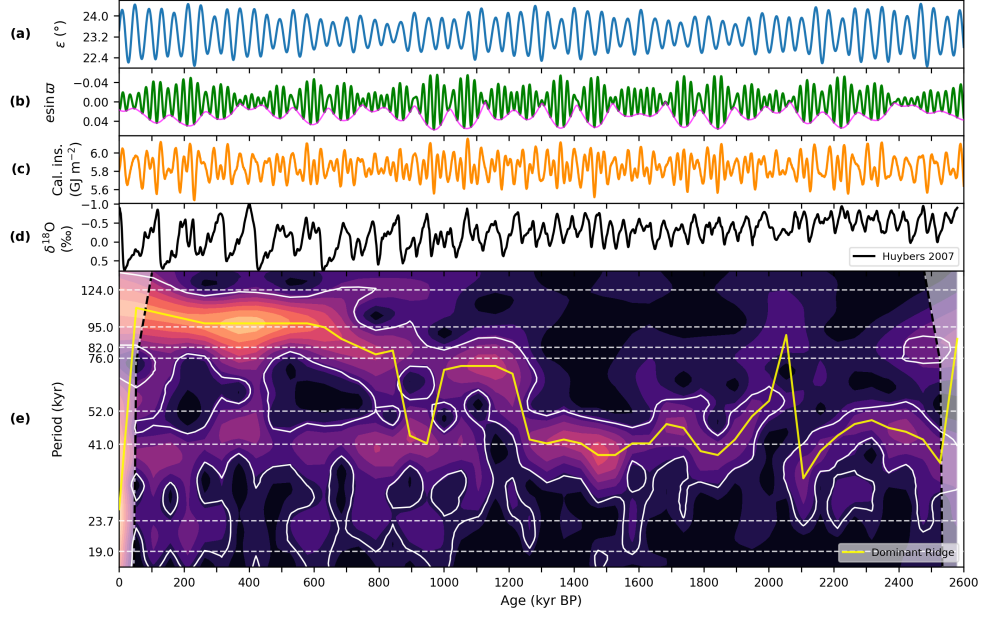


Fig. S6 Time-series and wavelet analyses of the benthic $\delta^{18}\text{O}$ stack record of Huybers (2007) [16], aligned with astronomical forcing [4] over the last 2.6 Myr. (a) Obliquity (ϵ). (b) Climatic precession ($e \sin \omega$, green) shown with its eccentricity envelope (e , magenta). (c) Caloric summer half-year insolation at 65°N [2, 3]. (d) The benthic $\delta^{18}\text{O}$ stack record of Huybers (2007) [16]. (e) Wavelet power scalogram of the $\delta^{18}\text{O}$ record. The yellow line indicates the ridge of maximum wavelet power. Areas enclosed by white dashed lines indicate power significant at the 95% confidence level against an AR(1) benchmark. Horizontal dashed lines denote major astronomical periodicities, including the 76-kyr and 52-kyr scales discussed in this study.

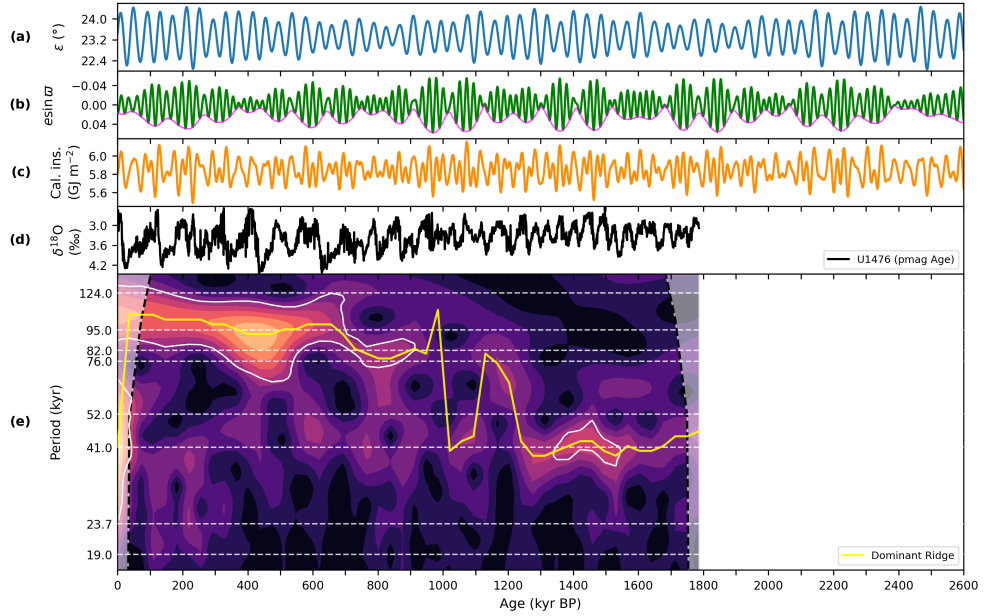


Fig. S7 Time-series and wavelet analyses of the benthic $\delta^{18}\text{O}$ record from U1476pMag [17], aligned with astronomical forcing [4] over the last 2.6 Myr. (a) Obliquity (ε). (b) Climatic precession ($e \sin \varpi$, green) shown with its eccentricity envelope (e , magenta). (c) Caloric summer half-year insolation at 65°N [2, 3]. (d) The benthic $\delta^{18}\text{O}$ record from U1476pMag [17]. (e) Wavelet power scalogram of the $\delta^{18}\text{O}$ record. The yellow line indicates the ridge of maximum wavelet power. Areas enclosed by white dashed lines indicate power significant at the 95% confidence level against an AR(1) benchmark. Horizontal dashed lines denote major astronomical periodicities, including the 76-kyr and 52-kyr scales discussed in this study.

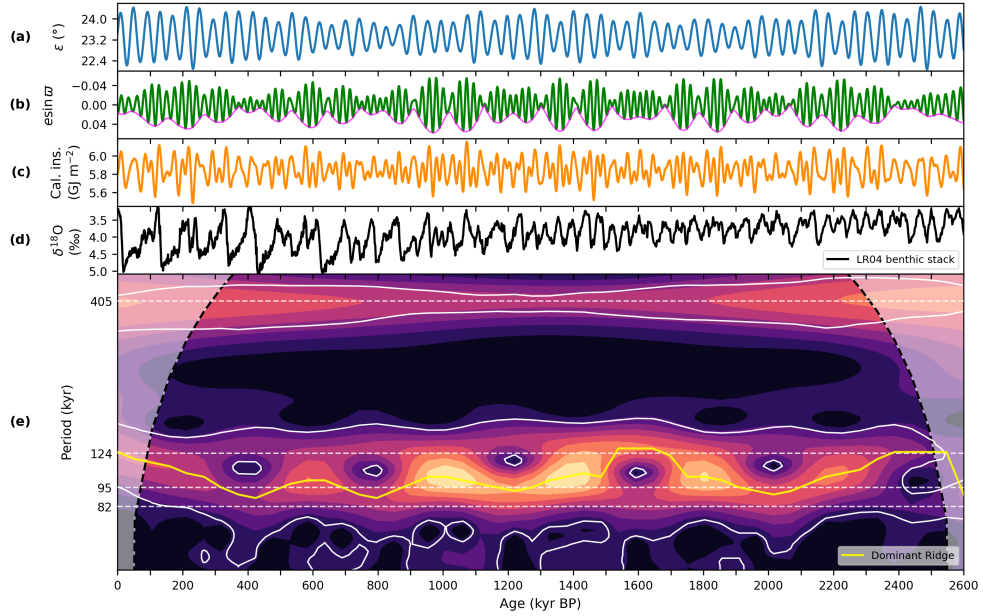


Fig. S8 Time-series and wavelet analyses of eccentricity, aligned with other astronomical elements [4] and the LR04 benthic $\delta^{18}\text{O}$ stack record over the last 2.6 Myr. (a) Obliquity (ϵ). (b) Climatic precession ($e \sin \varpi$, green) shown with its eccentricity envelope (e , magenta). (c) Caloric summer half-year insolation at 65°N [2, 3]. (d) LR04 benthic $\delta^{18}\text{O}$ stack record without orbital tuning. [12] (e) Wavelet power scalogram of eccentricity. The yellow line indicates the ridge of maximum wavelet power obtained by omitting the 405-kyr band. Areas enclosed by white dashed lines indicate power significant at the 95% confidence level against an AR(1) benchmark. Horizontal dashed lines denote major astronomical periodicities of eccentricity.

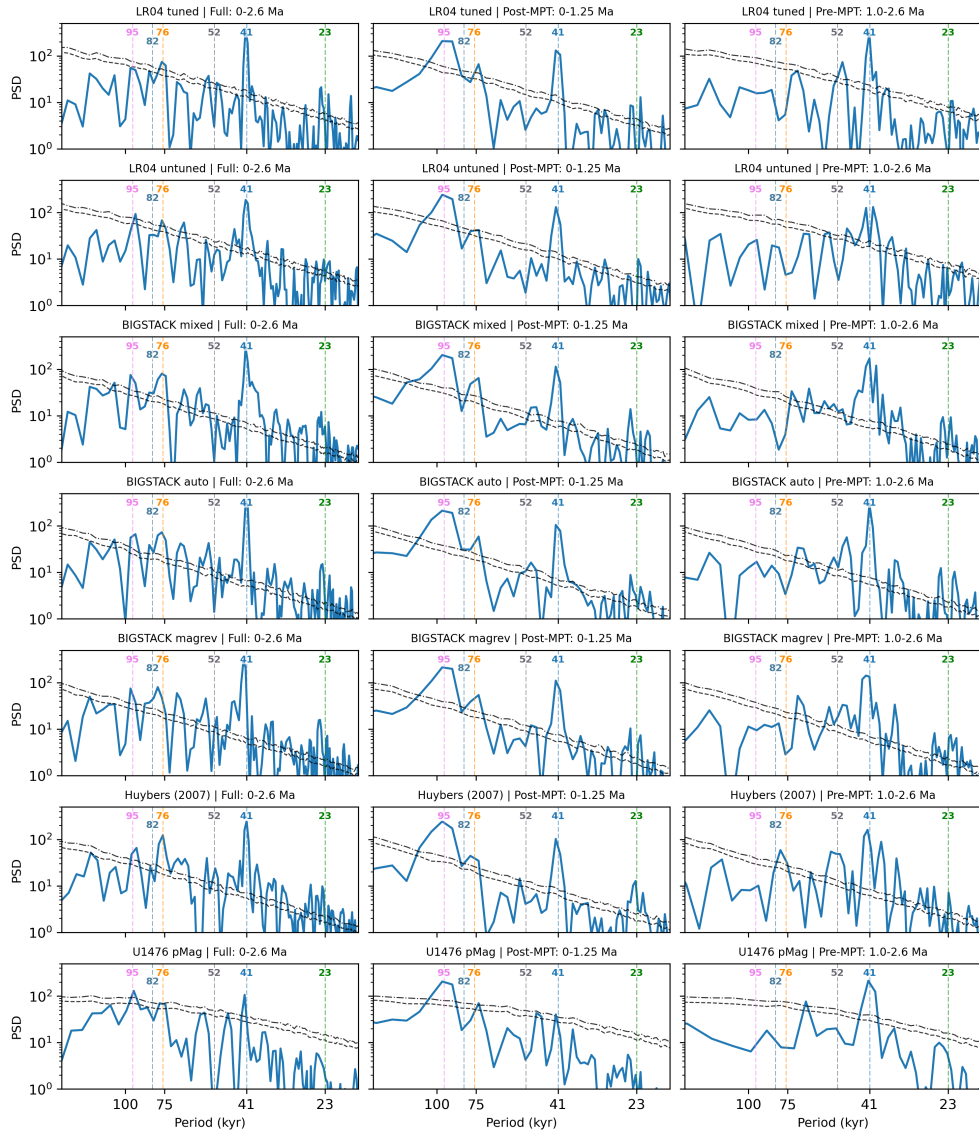


Fig. S9 Comparison of conventional periodograms across multiple benthic $\delta^{18}\text{O}$ records in Supplementary Information Fig. 1. Each column represents a specific time interval: the entire Quaternary (0–2.6 Ma; left), the mid-to-late Pleistocene (0–1.25 Ma; center), and the early Pleistocene (1.0–2.6 Ma; right). Blue lines indicate the PSD of the standardized $\delta^{18}\text{O}$ records, while dashed and dotted black lines denote the 95% and 90% confidence levels, respectively, against an AR(1) benchmark. Vertical dashed lines highlight key periodicities: the canonical eccentricity (95 kyr), obliquity (41 kyr), and precession (23 kyr) cycles, as well as the sub-harmonics analyzed in this study (82, 76, and 52 kyr). The time series is interpolated at 1-kyr intervals before the analysis and then linearly detrended over the analysis period. All analyses are performed using the `pyleoclim` (version 1.2.0) [18].

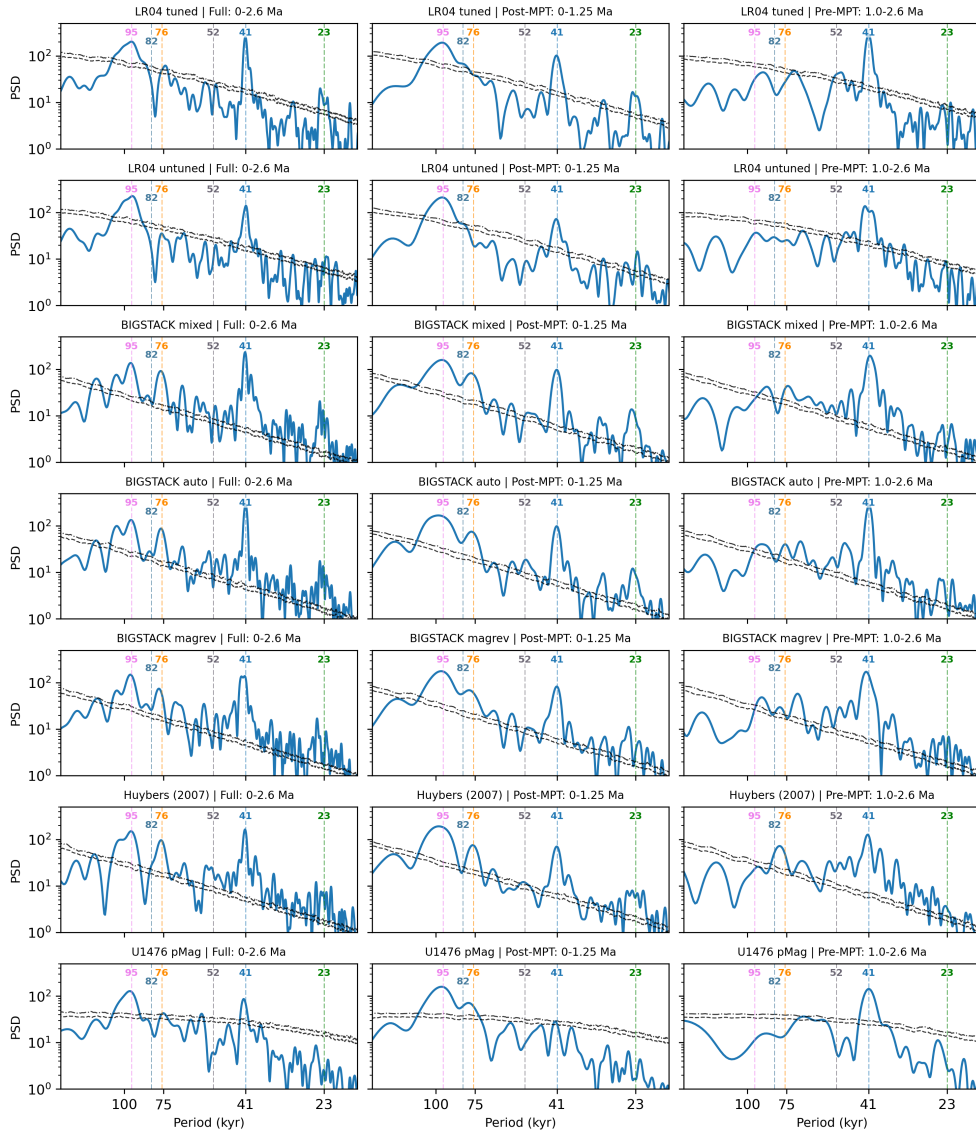


Fig. S10 Comparison of Lomb-Scargle spectra across multiple benthic $\delta^{18}\text{O}$ records in Supplementary Information Fig. 1. Each column represents a specific time interval: the entire Quaternary (0–2.6 Ma; left), the mid-to-late Pleistocene (0–1.25 Ma; center), and the early Pleistocene (1.0–2.6 Ma; right). Blue lines indicate the PSD of the standardized $\delta^{18}\text{O}$ records, while dashed and dotted black lines denote the 95% and 90% confidence levels, respectively, against an AR(1) benchmark. Vertical dashed lines highlight key periodicities: the canonical eccentricity (95 kyr), obliquity (41 kyr), and precession (23 kyr) cycles, as well as the sub-harmonics analyzed in this study (82, 76, and 52 kyr). The series are linearly detrended over the analysis period. All analyses are performed using the `pyleoclim` (version 1.2.0) [18].

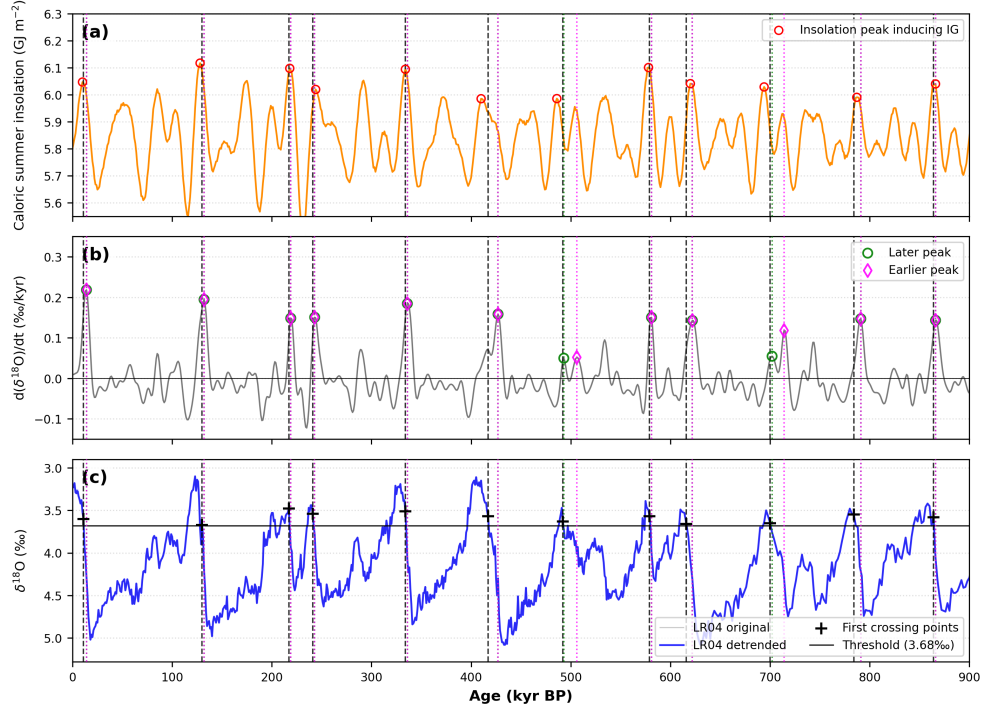


Fig. S11 Detailed deglaciation analysis and timing of interglacial onsets (0–900 ka). (a) Caloric summer insolation at 65°N [2, 3]. Red open circles denote the interglacial-inducing insolation peaks [1] (see Methods). (b) The rate of change in benthic $\delta^{18}\text{O}$ ($d(\delta^{18}\text{O})/dt$) derived from the 10-kyr smoothed LR04 $\delta^{18}\text{O}$ record. Green circles and magenta diamonds highlight the local maxima in the deglaciation rate, representing later and earlier phases of ice-sheet retreat, respectively. (c) Benthic $\delta^{18}\text{O}$ records from the LR04 stack. The original record (light gray) is shown alongside the detrended series [1] (blue line) used for threshold analysis (see Methods). Black crosses ('+') mark the first crossing points where the detrended $\delta^{18}\text{O}$ values exceed the 3.68‰ threshold, defining the onset of interglacial conditions. Vertical dashed lines (black) and dotted lines (green and magenta) indicate the timings of threshold crossings and peak deglaciation rates, respectively, highlighting the phase relationship between each insolation peak and climate response.

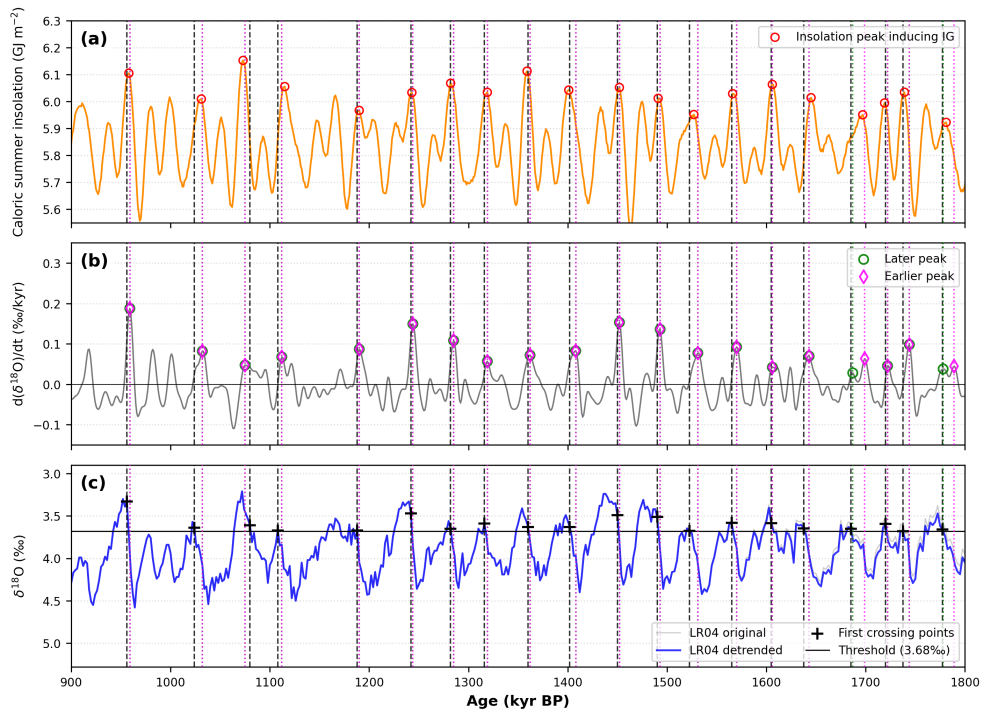


Fig. S12 Detailed deglaciation analysis and timing of interglacial onsets (900–1800 ka). See caption in Fig. S11.

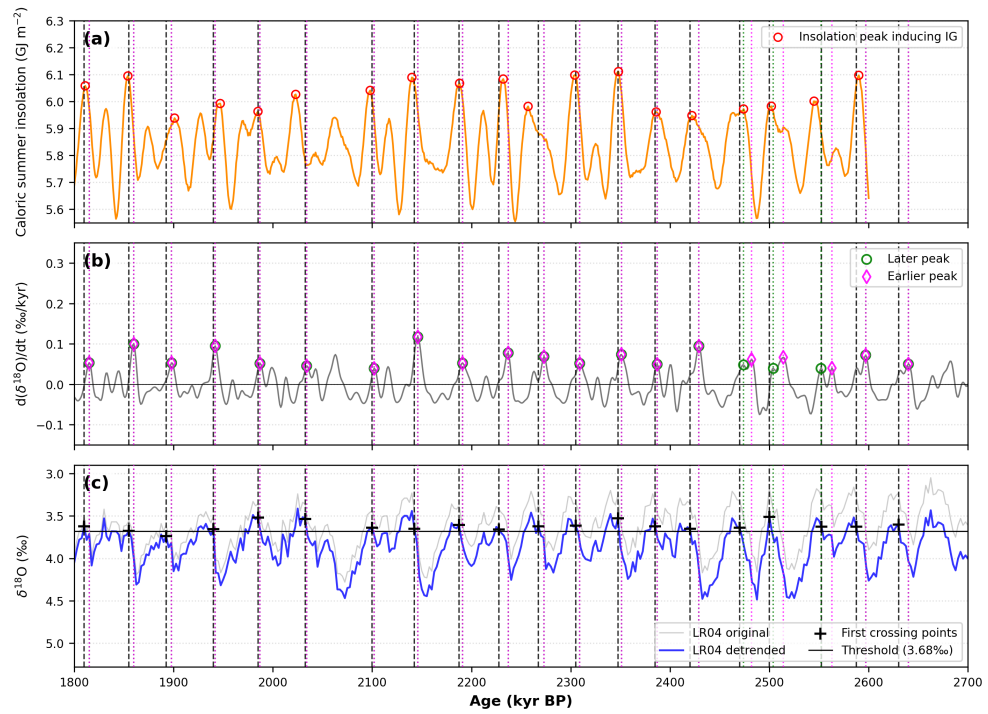


Fig. S13 Detailed deglaciation analysis and timing of interglacial onsets (1800–2700 ka). See caption in Fig. S11.

Relationship between Eccentricity and Precession Duration

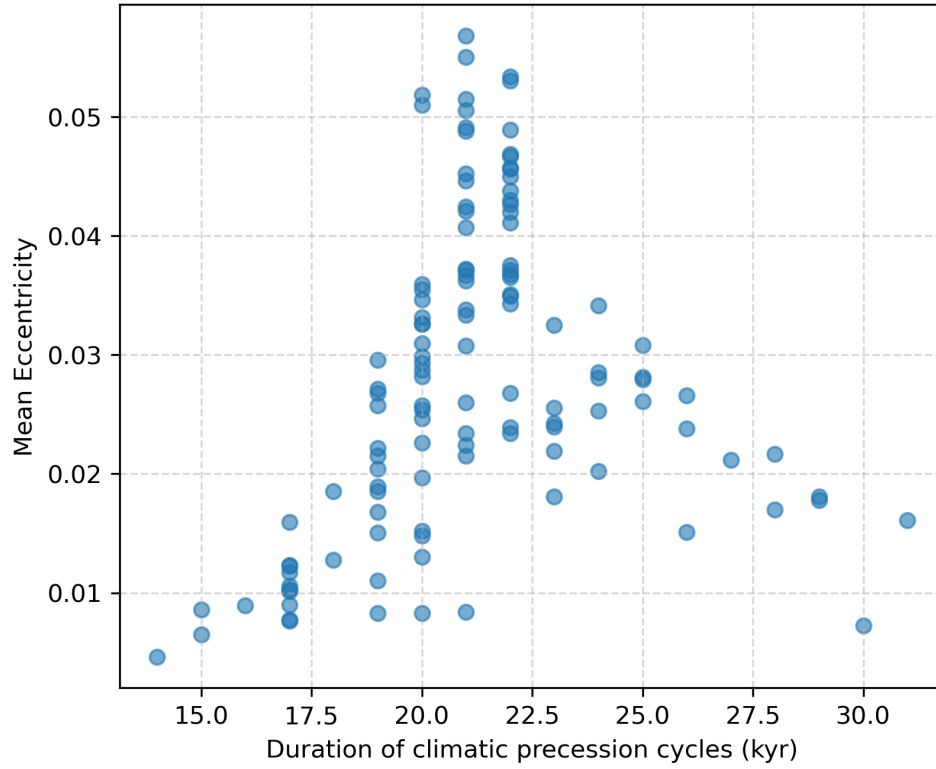


Fig. S14 Relationship between eccentricity and the duration of climatic precession cycles. The duration of climatic precession cycle is calculated from the spacing between successive precession minima. The local mean of eccentricity is calculated over successive precession minima.

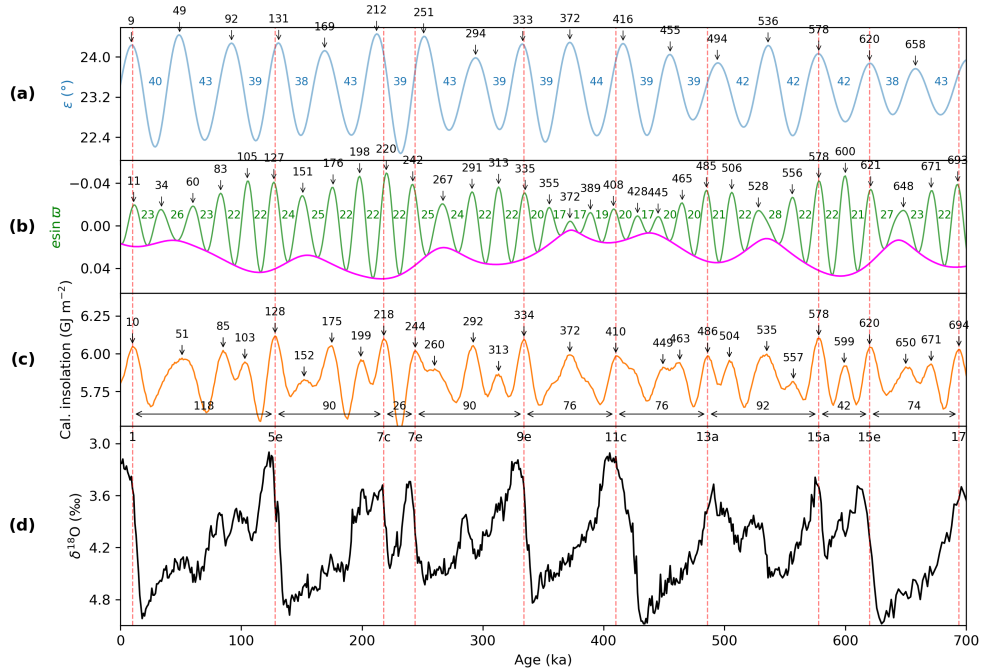


Fig. S15 Orbital forcing and glacial-interglacial cycles over the last 700 kyr. (a) Obliquity (ε) with peak ages (ka) indicated by arrows. Peak-to-peak spacings are shown in blue between consecutive peaks. (b) Climatic precession ($e \sin \omega$, green) and eccentricity (e , magenta). Note that the $e \sin \omega$ axis is inverted to align with insolation peaks. Peak-to-peak spacings are shown in green between consecutive minima. (c) Caloric summer half-year insolation at 65°N [2, 3]. Horizontal double-headed arrows indicate the interglacial spacings (T_{ins}), where values correspond to the spacings between interglacial-inducing insolation maxima. (d) LR04 $\delta^{18}\text{O}$ stack [11]. Numbers at the top denote Marine Isotope Stages (MIS). Vertical red dashed lines across all panels mark the timing of insolation peaks that induced interglacials [1]. The orbital solutions are from Laskar et al. (2004) [4].

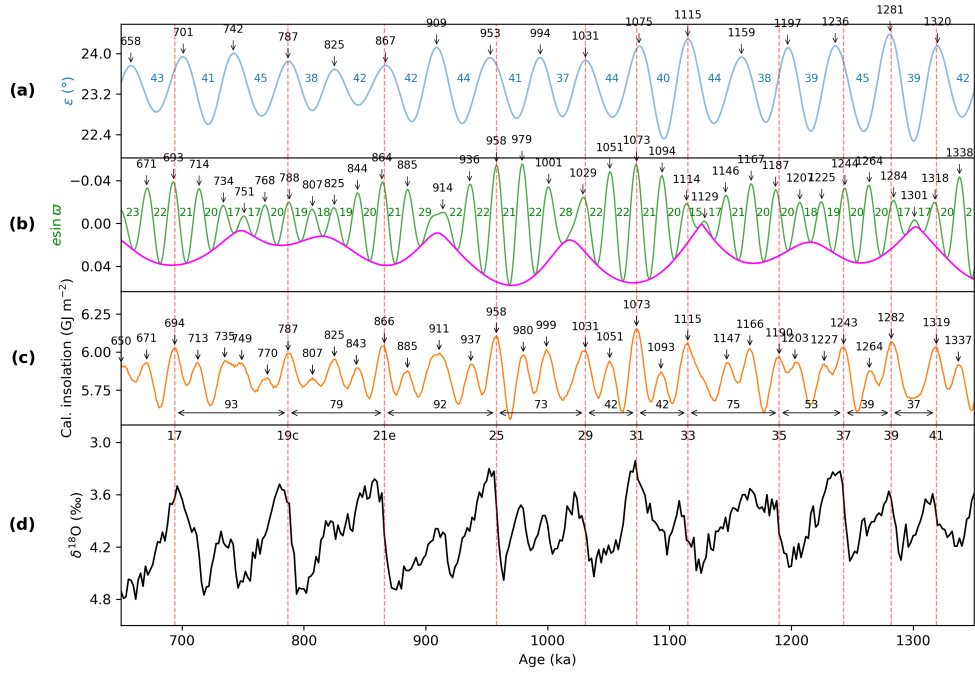


Fig. S16 Orbital forcing and glacial-interglacial cycles from 650 to 1350 ka. (a) Obliquity (ε) with peak ages (ka) indicated by arrows. Peak-to-peak spacings are shown in blue between consecutive peaks. (b) Climatic precession ($e \sin \varpi$, green) and eccentricity (e , magenta). Note that the $e \sin \varpi$ axis is inverted to align with insolation peaks. Peak-to-peak spacings are shown in green between consecutive minima. (c) Caloric summer half-year insolation at 65°N [2, 3]. Horizontal double-headed arrows indicate the interglacial spacings (T_{ins}), where values correspond to the spacings between interglacial-inducing insolation maxima. (d) LR04 $\delta^{18}\text{O}$ stack [11]. Numbers at the top denote Marine Isotope Stages (MIS). Vertical red dashed lines across all panels mark the timing of insolation peaks that induced interglacials [1]. The orbital solutions are from Laskar et al. (2004) [4].

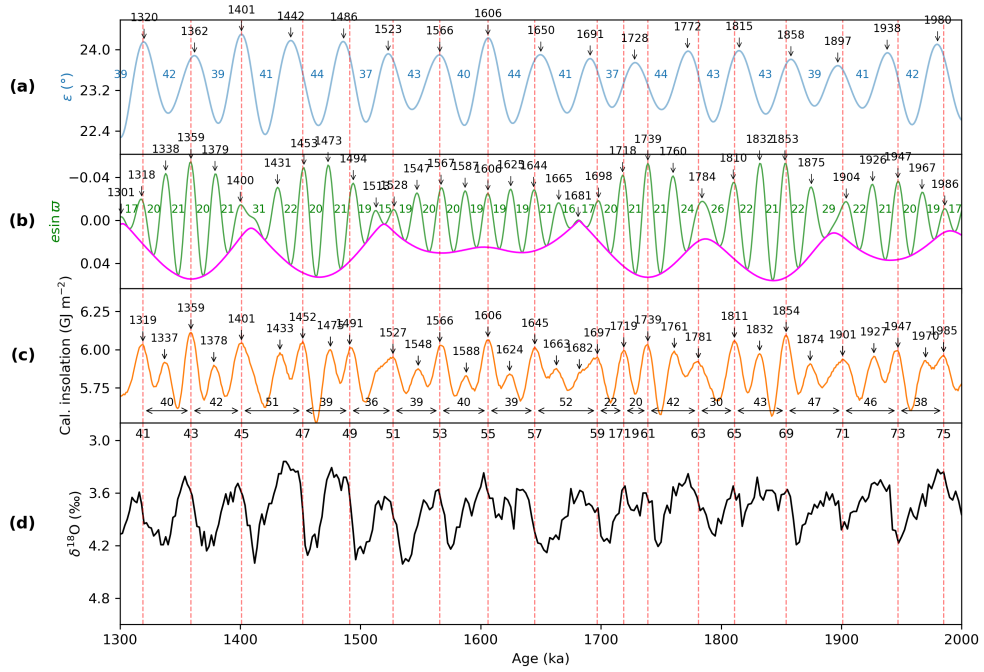


Fig. S17 Orbital forcing and glacial-interglacial cycles from 1300 to 2000 ka. (a) Obliquity (ϵ) with peak ages (ka) indicated by arrows. Peak-to-peak spacings are shown in blue between consecutive peaks. (b) Climatic precession ($e \sin \omega$, green) and eccentricity (e , magenta). Note that the $e \sin \omega$ axis is inverted to align with insolation peaks. Peak-to-peak spacings are shown in green between consecutive minima. (c) Caloric summer half-year insolation at 65°N [2, 3]. Horizontal double-headed arrows indicate the interglacial spacings (T_{ins}), where values correspond to the spacings between interglacial-inducing insolation maxima. (d) LR04 $\delta^{18}\text{O}$ stack [11]. Numbers at the top denote Marine Isotope Stages (MIS). Vertical red dashed lines across all panels mark the timing of insolation peaks that induced interglacials [1]. The orbital solutions are from Laskar et al. (2004) [4].

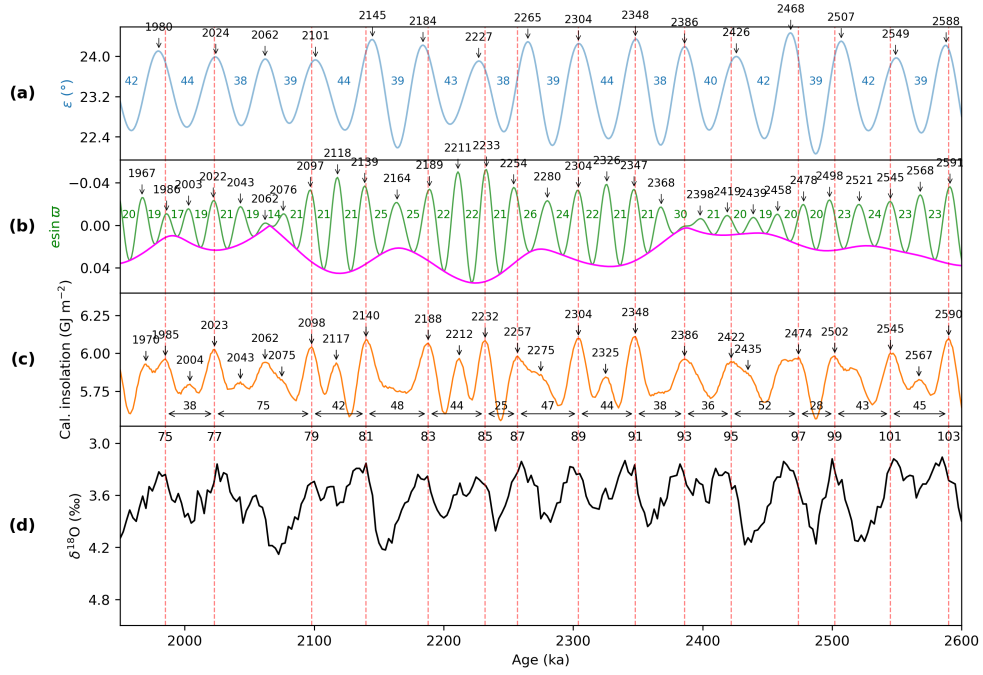


Fig. S18 Orbital forcing and glacial-interglacial cycles from 1950 to 2600 ka. (a) Obliquity (ε) with peak ages (ka) indicated by arrows. Peak-to-peak spacings are shown in blue between consecutive peaks. (b) Climatic precession ($e \sin \varpi$, green) and eccentricity (e , magenta). Note that the $e \sin \varpi$ axis is inverted to align with insolation peaks. Peak-to-peak spacings are shown in green between consecutive minima. (c) Caloric summer half-year insolation at 65°N [2, 3]. Horizontal double-headed arrows indicate the interglacial spacings (T_{ins}), where values correspond to the spacings between interglacial-inducing insolation maxima. (d) LR04 $\delta^{18}\text{O}$ stack [11]. Numbers at the top denote Marine Isotope Stages (MIS). Vertical red dashed lines across all panels mark the timing of insolation peaks that induced interglacials [1]. The orbital solutions are from Laskar et al. (2004) [4].

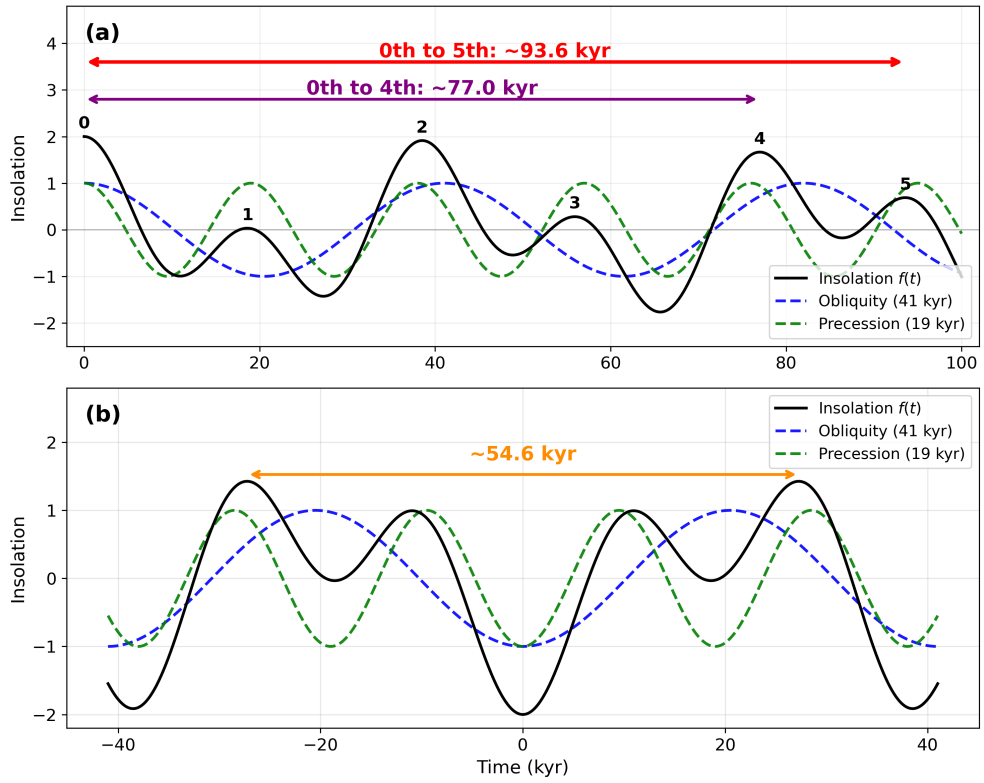


Fig. S19 Schematic representation of an insolation curve approximated by two harmonic components. The insolation curve is assumed to be represented as the sum of two harmonic components: $\cos(2\pi t/19)$ (climatic precession) and $\cos(2\pi t/41)$ (obliquity). (a) The insolation curve is given by $f(t) = \cos(2\pi t/19) + \cos(2\pi t/41)$. (b) The insolation curve is given by $f(t) = -\cos(2\pi t/19) - \cos(2\pi t/41)$.

Supporting Information Table S1 for "Beyond the 100-kyr and 41-kyr dichotomy: ~76- and ~52-kyr signals and forbidden periodicities in Quaternary glacial cycles" by Takahito Mitsui

Creator: Takahito Mitsui (Juntendo University). (email: takahito321ATgmail.com)

Date: 2 April 2026

Description:

This sheet shows the calculation of the insolation-based inter-deglaciation intervals (T_{ins}) by using the approximation formulae described in Supporting Information document.

The colitic summer half-year insolation at 65N is chosen as the insolation metric following Tzedakis et al. Nature (2017). It is calculated based on the orbital solution of Laskar et al. A&A (2004) using R-package 'Palinsol' created by Michel Crucifix.

The insolation-based inter-deglaciation interval (T_{ins}) between two interglacials (called "start" and "end" below) is approximately given by the spacing between two insolation peaks that induce interglacials.

Marine Isotope Stage (MIS) of interglacial "end"	Marine Isotope Stage (MIS) of interglacial "start"	Insolation peak "end" (ka)	Insolation peak "start" (ka)	Actual inter-deglaciation interval (T_{ins}) (kyr)	Precession (esin) peak "end" (ka)	Precession (esin) peak "start" (ka)	Number of precession cycles	Local-mean precession period T_p (kyr)	Obliquity peak "end" (ka)	Obliquity peak "start" (ka)	Number of obliquity cycles	Local-mean obliquity period (kyr)	Formula type	Predicted Inter-deglaciation interval (T_{ins}) (kyr)	Difference = predicted T_{ins} - actual T_{ins} (kyr)	T_{later} (kyr)	$T_{earlier}$ (kyr)
1	5e	10	128	118	11	127	5	23.2	9	131	3	40.66666667	5a	117.4095046	-0.590495389	118	118
5e	7c	128	218	90	127	220	4	23.25	131	212	2	40.5	4a	90.75253717	0.752537167	87	87
7c	7e	218	244	26	220	242	1	22	212	251	1	39	1b	25.63885892	-0.36114108	24	24
7e	9e	244	334	90	242	335	4	23.25	251	333	2	41	4a	90.8365547	0.83655466	93	93
9e	11c	334	410	76	335	408	4	18.25	333	416	2	41.5	4a	74.26141357	-1.738586426	91	91
11c	13a	410	486	76	408	485	4	19.25	416	494	2	39	pp	77	1	66	79
13a	15a	486	578	92	485	578	4	23.25	494	578	2	42	4a	91.13043353	-0.86956647	88	75
15a	15e	578	620	42	578	621	2	21.5	578	620	1	42	2a	42.7926566	0.792656604	41	41
15e	17	620	694	74	621	693	3	24	620	701	2	40.5	3a	74.10102939	0.101029386	80	92
17	19c	694	787	93	693	788	5	19	701	787	2	43	5a	93.76811957	0.768119566	89	77
19c	21e	787	866	79	788	864	4	19	787	867	2	40	4b	76.73089134	-2.26910866	75	75
21e	25	866	958	92	864	958	4	23.5	867	953	2	43	4a	92.31555016	0.315550159	93	93
25	29	958	1031	73	958	1029	3	23.66666667	953	1031	2	39	3a	72.7835095	-0.216490502	73	73
29	31	1031	1073	42	1029	1073	2	22	1031	1075	1	44	2a	44	2	43	43
31	33	1073	1115	42	1073	1114	2	20.5	1075	1115	1	40	2a	40.79230366	-1.207696343	37	37
33	35	1115	1190	75	1114	1187	4	18.25	1115	1197	2	41	4a	74.22310319	-0.776896814	78	78
35	37	1190	1243	53	1187	1244	3	19	1197	1236	1	39	3b	54.1564265	1.156426499	54	54
37	39	1243	1282	39	1244	1284	2	20	1236	1281	1	45	pp	40	1	41	41
39	41	1282	1319	37	1284	1318	2	17	1281	1320	1	39	2b	34.78698727	-2.213012733	34	34
41	43	1319	1359	40	1318	1359	2	20.5	1320	1362	1	42	pp	41	1	43	43
43	45	1359	1401	42	1359	1400	2	20.5	1362	1401	1	39	pp	41	-1	46	46
45	47	1401	1452	51	1400	1453	2	26.5	1401	1442	1	41	2a	50.04423465	-0.955765345	44	44
47	49	1452	1491	39	1453	1494	2	20.5	1442	1486	1	44	2c	39.73163334	0.731633338	41	41
49	51	1491	1527	36	1494	1528	2	17	1486	1523	1	37	pp	34	-2	38	38
51	53	1527	1566	39	1528	1567	2	19.5	1523	1566	1	43	2a	39.6628726	0.662872597	39	39
53	55	1566	1606	40	1567	1606	2	19.5	1566	1606	1	40	2a	39.19168569	-0.808314308	36	36
55	57	1606	1645	39	1606	1644	2	19	1606	1650	1	44	2a	38.87946221	-0.12053779	37	37
57	59	1645	1697	52	1644	1698	3	18	1650	1691	1	41	3b	52.08886632	0.088866322	44	56
59	1719	1697	1719	22	1698	1718	1	20	1691	1728	1	37	1c	21.5508926	-0.449107399	35	23
1719	61	1719	1739	20	1718	1739	1	21	1728	1728	0	#DIV/0!	pp	21	1	22	22
61	63	1739	1781	42	1739	1784	2	22.5	1728	1772	1	44	2c	43.11739279	1.117392788	34	45
63	65	1781	1811	30	1784	1810	1	26	1772	1815	1	43	1b	30.23605565	0.236055654	37	2
65	69	1811	1854	43	1810	1853	2	21.5	1815	1858	1	43	pp	43	0	45	45
69	71	1854	1901	47	1853	1904	2	25.5	1858	1897	1	39	2b	47.48572001	0.485720005	38	38
71	73	1901	1947	46	1904	1947	2	21.5	1897	1938	1	41	2d	44.86553125	-1.134468748	44	44
73	75	1947	1985	38	1947	1986	2	19.5	1938	1980	1	42	2c	37.81281134	-0.187188656	45	45
75	77	1985	2023	38	1986	2022	2	18	1980	2024	1	44	2b	37.11082651	-0.889173493	47	47
77	79	2023	2098	75	2022	2097	4	18.75	2024	2101	2	38.5	4b	75.38269763	0.382697632	68	68
79	81	2098	2140	42	2097	2139	2	21	2101	2145	1	44	pp	42	0	44	44
81	83	2140	2188	48	2139	2189	2	25	2145	2184	1	39	2b	46.86370843	-1.136291572	45	45
83	85	2188	2232	44	2189	2233	2	22	2184	2227	1	43	2b	43.79261153	-0.207388473	46	46
85	87	2232	2257	25	2233	2254	1	21	2227	2265	1	38	1b	24.46929504	-0.53070496	3	36
87	89	2257	2304	47	2254	2304	2	25	2265	2304	1	39	2a	47.27718819	0.277188193	36	36
89	91	2304	2348	44	2304	2347	2	21.5	2304	2348	1	44	2a	43.19246791	-0.807532094	42	42
91	93	2348	2386	38	2347	2398	2	25.5	2348	2386	1	38	O2-(P1+C)	38.5	0.5	36	36
93	95	2386	2422	36	2398	2419	1	21	2386	2426	1	40	(O2+P2)/	36.5	0.5	42	42
95	97	2422	2474	52	2419	2478	3	19.66666667	2426	2468	1	42	3b*	51.96142631	-0.038573691	45	53
97	99	2474	2502	28	2478	2498	1	20	2468	2507	1	39	1b*	27.94484616	-0.055153836	30	32
99	101	2502	2545	43	2498	2545	2	23.5	2507	2549	1	42	2c	45.05090417	2.050904171	48	49
101	103	2545	2590	45	2545	2591	2	23	2549	2588	1	39	2b	44.21662793	-0.78337207	45	34

Note: Special rules are employed for MIS 99-97, 97-95, 95-93, and 93-91, where eccentricity is particularly low. See Supplementary Note.